



1 **Iron from coal combustion particles dissolves much faster than** 2 **mineral dust under simulated atmospheric acid conditions**

3 Clarissa Baldo¹, Akinori Ito², Michael D. Krom^{3,4}, Weijun Li⁵, Tim Jones⁶, Nick Drake⁷, Konstantin
4 Ignatyev⁸, Nicholas Davidson¹, Zongbo Shi¹

5 ¹School of Geography Earth and Environmental Sciences, University of Birmingham, Birmingham, United Kingdom

6 ²Yokohama Institute for Earth Sciences, JAMSTEC, Yokohama, Kanagawa 236-0001, Japan

7 ³Morris Kahn Marine Station, Charney School of Marine Sciences, University of Haifa, Haifa, Israel

8 ⁴School of Earth and Environment, University of Leeds, Leeds, United Kingdom

9 ⁵Department of Atmospheric Sciences, School of Earth Sciences, Zhejiang University, Hangzhou 310027, China

10 ⁶School of Earth and Environmental Sciences, Cardiff University, Cardiff, United Kingdom

11 ⁷Department of Geography, King's College London, London, United Kingdom

12 ⁸Diamond Light Source, Didcot, Oxfordshire, United Kingdom

13 *Correspondence to:* Zongbo Shi (z.shi@bham.ac.uk); Akinori Ito (akinori@jamstec.go.jp)

14 **Abstract.** Mineral dust is the largest source of aerosol iron (Fe) to the offshore global ocean, but acidic processing of coal fly
15 ash (CFA) in the atmosphere may result in a disproportionately higher contribution of bioavailable Fe. Here, we determined the
16 Fe speciation and dissolution kinetics of CFA from Aberthaw (United Kingdom), Krakow (Poland), and Shandong (China) in
17 solutions which simulate atmospheric acidic processing. In CFA-PM₁₀ fractions, 8%-21.5% of the total Fe was as hematite
18 and goethite (dithionite extracted Fe), 2%-6.5 % as amorphous Fe (ascorbate extracted Fe), while magnetite (oxalate extracted
19 Fe) varied from 3%-22%. The remaining 50%-87 % of Fe was associated with aluminosilicates. High concentration of
20 ammonium sulphate ((NH₄)₂SO₄), often found in wet aerosols, increased Fe solubility of CFA up to 7 times at low pH (2-3).
21 Our results showed a large variability in the effects of oxalate on the Fe dissolution rates at pH 2, from no impact in Shandong
22 ash to doubled dissolution in Krakow ash. However, this enhancement was suppressed in the presence of high concentration
23 of (NH₄)₂SO₄. Dissolution of highly reactive Fe was insufficient to explain the high Fe solubility at low pH in CFA, and the
24 modelled dissolution kinetics suggests that other Fe phases such as magnetite may also dissolve rapidly under acidic conditions.
25 Overall, Fe in CFA dissolved up to 7 times faster than in Saharan dust samples at pH 2. Based on these laboratory data, we
26 developed a new scheme for the proton- and oxalate- promoted Fe dissolution of CFA, which was implemented into the global
27 atmospheric chemical transport model IMPACT. The revised model showed a better agreement with observations of surface
28 concentration of dissolved Fe in aerosol particles over the Bay of Bengal, due to the rapid Fe release at the initial stage at
29 highly acidic conditions. The improved model also enabled us to predict sensitivity to a more dynamic range of pH changes,
30 particularly between anthropogenic combustion and biomass burning aerosols.

31



32 1 Introduction

33 The availability of iron (Fe) limits primary productivity in high-nutrient low-chlorophyll (HNLC) regions of the global ocean
34 including the subarctic North Pacific, the East Equatorial Pacific and the Southern Ocean (Boyd et al., 2007; Martin, 1990). In
35 other regions of the global ocean such as the subtropical North Atlantic, the Fe input may affect primary productivity by
36 stimulating nitrogen fixation (Mills et al., 2004; Moore et al., 2006). These areas are particularly sensitive to changes in the
37 supply of bioavailable Fe. Atmospheric aerosols are an important source of soluble (and, thus potentially bioavailable) Fe to
38 the offshore global ocean. The deposition of bioavailable Fe to the ocean can alter biogeochemical cycles and increase the
39 carbon uptake, consequently affecting the climate (e.g., Jickells and Moore, 2015; Jickells et al., 2005; Kanakidou et al., 2018;
40 Mahowald et al., 2010; Shi et al., 2012). In general, bioavailable Fe consists of aerosol dissolved Fe, and Fe-nanoparticles
41 which can be present in the original particulate matter and/or formed during atmospheric transport as a result of cycling into
42 and out of clouds (Shi et al., 2009). It is in addition possible that other more refractory forms of Fe could be solubilised in the
43 surface waters by zooplankton (Schlosser et al., 2018) or the microbial community (Rubin et al., 2011).

44 Atmospheric Fe is largely derived from lithogenic sources, which contribute around 95% of the total Fe in suspended particles
45 (e.g., Myriokefalitakis et al., 2018) and hence most studies concentrate on atmospheric processing of mineral dust (e.g.,
46 Cwiertny et al., 2008; Fu et al., 2010; Ito and Shi, 2016; Shi et al., 2011a; Shi et al., 2015). Mineral dust has low Fe solubility
47 (dissolved Fe/ total Fe) near the source regions, generally below 0.5% (e.g., Schroth et al., 2009; Shi et al., 2011c), increasing
48 somewhat as a result of atmospheric processing (e.g., Baker et al., 2021; Baker et al., 2020). Other sources of bioavailable Fe
49 to the ocean are from combustion sources such as biomass burning, coal combustion and oil combustion (e.g., shipping
50 emissions) (e.g., Ito et al., 2018; Rathod et al., 2020). Although these sources are only a small fraction of the total Fe in
51 atmospheric particulates, the Fe solubility of pyrogenic sources can be 1–2 orders of magnitude higher than in mineral dust,
52 and thus can be important in promoting carbon uptake. However the Fe solubility of these sources vary considerably depending
53 on the particular sources with higher values observed for oil combustion and biomass burning (Ito et al., 2021b and references
54 therein).

55 Wang et al. (2015) estimated that coal combustion produces around $\sim 0.9 \text{ Tg yr}^{-1}$ of atmospheric Fe (on average for 1960–
56 2007), contributing up to $\sim 86\%$ of the total anthropogenic Fe emissions. A more recent study, which has included metal
57 smelting as atmospheric Fe source, estimated that coal combustion emitted $\sim 0.7 \text{ Tg yr}^{-1}$ of Fe for the year 2010, contributing
58 around 34% of the total anthropogenic Fe (Rathod et al., 2020). Although the use of coal as a principle energy source has been
59 recently reduced as a result of concern about air quality and global warming, coal is still an important energy source in a
60 number of countries in particular in the Asia-Pacific region (BP, 2020). In China, most of the total energy is supplied by coal,
61 contributing over 50% of the global coal consumption in 2019, followed by India (12%), and the US (8%). Germany and
62 Poland are the largest coal consumers in Europe, accounting together for around 40% of the European usage (BP, 2020). South
63 Africa is also among the principal countries for coal consumption (BP, 2020) and is a source of particles to the Fe-limited
64 Southern Ocean (e.g., Ito et al., 2019).

65 Coal fly ash (CFA) is a by-product of coal combustion. This generally consists of glassy spherical particles (e.g., Brown et al.,
66 2011), which are formed through different transformations (decomposition, fusion, agglomeration, volatilization) of mineral
67 matter in coal during combustion (e.g., Jones, 1995), and are transported with the flue gases undergoing rapid solidification.
68 CFA are co-emitted with acidic gases such as sulphur dioxide (SO_2), nitrogen oxides (NO_x) and carbon dioxide (CO_2) (e.g.,
69 Munawar, 2018).

70 During long-range transport, CFA particles undergo atmospheric processing with the CFA surface coated by acidic species
71 such as sulphuric acid (H_2SO_4) and oxalic acid ($\text{H}_2\text{C}_2\text{O}_4$) in atmospheric aerosols. Aged CFA particles are hygroscopic and



72 absorb water at typical relative humidity in the marine atmosphere. This forms a thin layer of water with high acidity, low pH
73 and high ionic strength (Meskhidze et al., 2003; Spokes and Jickells, 1995; Zhu et al., 1992). In addition, ammonia (NH_3)
74 which is a highly hydrophilic gas, can also partition into the aerosol phase, react with H_2SO_4 and form ammonium sulphate
75 ($(\text{NH}_4)_2\text{SO}_4$) an important inorganic salt contributing to the high ionic strength in such atmospheric aerosols (Seinfeld and
76 Pandis, 2016).

77 At low pH conditions, Fe solubility in aerosols increases, as the high concentration of protons (H^+) weakens the Fe-O bonds
78 facilitating the detachment of Fe from the surface lattice (Furrer and Stumm, 1986). Li et al. (2017) provided the first
79 observational evidence to confirm that the acidification leads to the release of Fe from anthropogenic particles.

80 In addition to these inorganic processes, organic ligands can also enhance atmospheric Fe dissolution by forming soluble
81 complexes with Fe (e.g., Cornell and Schwertmann, 2003). For example, $\text{H}_2\text{C}_2\text{O}_4$ is an important organic species in
82 atmospheric aerosols (e.g., Kawamura and Bikkina, 2016). Laboratory studies have demonstrated that $\text{H}_2\text{C}_2\text{O}_4$ increases Fe
83 solubility of atmospheric aerosol sources (Chen and Grassian, 2013; Paris and Desboeufs, 2013; Paris et al., 2011; Xu and
84 Gao, 2008). Recently, observations over the Bay of Bengal indicate that $\text{H}_2\text{C}_2\text{O}_4$ contributes to the increase in atmospheric
85 water dissolved Fe (Bikkina et al., 2020).

86 To simulate the Fe dissolution in CFA, it is necessary to determine the dissolution kinetics under realistic conditions. Previous
87 studies have investigated the Fe dissolution kinetics of CFA under acidic conditions. Chen et al. (2012) simulated acidic and
88 cloud processing of certified CFA. Fu et al. (2012) determined the dissolution kinetics of CFA samples at pH 2, while Chen
89 and Grassian (2013) investigated the effect of organic species (e.g., oxalate and acetate) at pH 2-3. These studies showed that
90 high acidity and the presence of oxalate enhanced Fe dissolution, similar to those reported in mineral dust (Chen et al., 2012;
91 Chen and Grassian, 2013; Fu et al., 2012; Ito and Shi, 2016; Shi et al., 2011a). They also demonstrated that there are large
92 differences in dissolution rates in different types of CFA, likely related to Fe speciation.

93 Furthermore, high ionic strength, commonly seen in aerosol water, affects the activity of molecular species present in solution,
94 consequently it can significantly impact the Fe dissolution behaviour. Recent studies have considered the effect of the high
95 ionic strength on the Fe dissolution kinetic of CFA under acidic conditions. For example, the Fe solubility of CFA samples
96 was measured at pH 1-2 with high sodium chloride (NaCl) concentrations (Borgatta et al., 2016), and with high sodium nitrate
97 (NaNO_3) concentrations Kim et al. (2020). In real atmospheric conditions, NaCl or NaNO_3 are unlikely to be the main driver
98 of high ionic strength in aged CFA. Although NaCl can coagulate with dust particles in the marine boundary layer (Zhang et
99 al., 2003), the aging of coal fly ash is primarily by the uptake of secondary species, particularly sulphate and ammonia (Li et
100 al., 2003). Ito and Shi (2016) found that at low pH and high concentration of $(\text{NH}_4)_2\text{SO}_4$ the Fe solubility of mineral dust is
101 likely to be enhanced by the adsorption of sulphate ions on the particle surface. However, to date the effect of high $(\text{NH}_4)_2\text{SO}_4$
102 concentrations on the Fe dissolution behaviour in combustion sources in the presence or absence of oxalate remains unknown.

103 The dissolution kinetics measured by Chen and Grassian (2013) has been used to develop a modelled dissolution scheme for
104 CFA, assuming a single Fe phase in CFA (Ito, 2015). However, there are multiple Fe phases in CFA, primarily hematite,
105 magnetite and Fe in aluminium silicate glass (Brown et al., 2011; Chen et al., 2012; Fu et al., 2012; Kukier et al., 2003; Kutchko
106 and Kim, 2006; Lawson et al., 2020; Sutto, 2018; Valeev et al., 2019; Waanders et al., 2003; Wang, 2014; Zhao et al., 2006),
107 but also accessory Fe-bearing minerals for example silicates, carbonate, sulphides and sulphates (Zhao et al., 2006). These
108 phases have a range of reactivities. Previous studies showed that CFA dissolves much faster during the first 1-2 hours than
109 subsequently (Borgatta et al., 2016; Chen et al., 2012; Chen and Grassian, 2013; Fu et al., 2012; Kim et al., 2020), confirming
110 the large difference in Fe dissolution from different phases.



111 In this study, laboratory experiments were conducted to determine the dissolution kinetics of coal combustion sources (e.g.,
112 coal fly ash) during simulated atmospheric acidic processing in the presence of $(\text{NH}_4)_2\text{SO}_4$ and oxalate which are commonly
113 found in atmospheric aerosols. In particular, we investigated the effect of high $(\text{NH}_4)_2\text{SO}_4$ concentrations on the proton-
114 promoted and oxalate-promoted Fe dissolution at low pH conditions. Our study also determined the Fe phases present in the
115 CFA and compared them to those present in mineral dust. The experimental results enabled us to develop a new Fe release
116 scheme for CFA sources which was then implemented into the global atmospheric chemical transport model IMPACT. The
117 model results were compared with observations of surface concentration of dissolved Fe in aerosol particles over the Bay of
118 Bengal from Bikkina et al. (2020).

119 2 Materials and Methods

120 2.1 Sample collection and subsequent size fractionation

121 CFA samples were collected from the electrostatic precipitators at three coal-fired power stations at different locations: United
122 Kingdom (Aberthaw ash), Poland (Krakow ash), and China (Shandong ash). The bulk samples were resuspended to obtain
123 dust fractions representative of particles emitted into the atmosphere. A custom-made resuspension system was used to collect
124 the PM_{10} fraction (particles with an aerodynamic diameter smaller than $10\ \mu\text{m}$), which is shown in Fig. S1. Around 20 g of
125 sample was placed into a glass bottle and injected at regular intervals (2-5 sec) into a glass reactor ($\sim 70\ \text{L}$) by flushing the
126 bottle with pure nitrogen. The air in the reactor was pumped at a flow rate of $30\ \text{L}\ \text{min}^{-1}$ into a PM_{10} sampling head. Particles
127 were collected on $0.6\ \mu\text{m}$ polycarbonate filters and transferred into centrifuge tubes. The system was cleaned manually and
128 flushed for 10 min with pure nitrogen before loading a new sample. A soil sample from Libya (Soil 5, 32.29237N/22.30437E)
129 was dry sieved to $63\ \mu\text{m}$ (which is referred to as Libya dust) and used for the comparison of CFA with mineral dust.

130 2.2 Fe dissolution kinetics

131 The Fe dissolution kinetics of the CFA samples was determined by time-dependent leaching experiments. We followed a
132 similar methodology as in Ito and Shi (2016). PM_{10} fractions were exposed to H_2SO_4 solutions at pH 1, 2 or 3, in the presence
133 of $\text{H}_2\text{C}_2\text{O}_4$ and/or $(\text{NH}_4)_2\text{SO}_4$ to simulate acidic processing in aerosol conditions. The concentration of $\text{H}_2\text{C}_2\text{O}_4$ in the
134 experiment solutions was chosen based on the molar ratio of oxalate and sulphate in $\text{PM}_{2.5}$ (particles with an aerodynamic
135 diameter smaller than $2.5\ \mu\text{m}$) from observations over the East Asia region (Yu et al., 2005). Around 50 mg of CFA was
136 leached in 50 ml of acidic solution to obtain a dust/liquid ratio of $1\ \text{g}\ \text{L}^{-1}$. The sample solution was mixed continuously on a
137 rotary mixer, in the dark at room temperature. A volume of 0.5 mL was sampled at fixed time intervals (2.5, 15, 60 min and 2,
138 6, 24, 48, 72, and 168 hours after the CFA sample was added to the experiment solution) and filtered through $0.2\ \mu\text{m}$ pore size
139 syringe filters. The dissolved Fe concentration in the filtrate was determined using the ferrozine method (Viollier et al., 2000).
140 Leaching experiments were also conducted on the Libya dust. The relative standard deviation (RSD) at each sampling time
141 varied from 4 % to 15 % ($n=7$).

142 The pH of all the experiment solutions was calculated using the E-AIM model III for aqueous solutions (Wexler and Clegg,
143 2002). In part this was because the high ionic strength generated by the elevated concentration of $(\text{NH}_4)_2\text{SO}_4$ prevents
144 electrochemical sensors from making accurate pH measurements. For the experiment solutions with no $(\text{NH}_4)_2\text{SO}_4$, the pH
145 was measured by a pH meter before adding the ash and at the end of the experiments. The solution pH increased after adding
146 the ash, and the change in pH was used to estimate the buffer capacity of alkaline minerals in the samples, including for
147 example calcium carbonates (CaCO_3), lime (CaO), and portlandite ($\text{Ca}(\text{OH})_2$). The estimated concentration of H^+ buffered was
148 used to input the concentration of H^+ into the E-AIM model. For each experiment, the pH was calculated before adding the
149 CFA samples and at the end of the experiments. The pH of the original solution before adding the samples was estimated from



150 the molar concentrations (mol L^{-1}) of H_2SO_4 , $\text{H}_2\text{C}_2\text{O}_4$ and $(\text{NH}_4)_2\text{SO}_4$ used to prepare the solution. The model inputs included
151 the total concentrations of H^+ (without $\text{H}_2\text{C}_2\text{O}_4$ contribution), NH_4^+ , SO_4^{2-} and $\text{H}_2\text{C}_2\text{O}_4$. For the experiment solutions with no
152 $(\text{NH}_4)_2\text{SO}_4$, we calculated the final pH by reducing the total H^+ concentration input into the model to match the pH measured
153 at the end of the experiments. The buffered H^+ was then estimated from the difference between the original and final H^+
154 concentration input into the model. To determine the final pH of the solutions with high ionic strength, the H^+ concentration
155 input in the model was calculated as the difference between the H^+ concentration in the original solution and the buffered H^+
156 estimated at low ionic strength.

157 For the solution with no $(\text{NH}_4)_2\text{SO}_4$, the difference between calculated and measured pH is $<7\%$. Table S1 reports the
158 concentrations of H_2SO_4 , $\text{H}_2\text{C}_2\text{O}_4$ and $(\text{NH}_4)_2\text{SO}_4$ in the experiment solutions, the original and final pH from model estimates
159 (including H^+ concentrations and activities), and the pH measurements for the solution with low ionic strength.

160 2.3 Sequential extractions

161 The content of Fe oxide species in the samples was determined by Fe sequential extraction (Baldo et al., 2020; Poulton and
162 Canfield, 2005; Raiswell et al., 2008; Shi et al., 2011b). The Fe oxide species included highly reactive amorphous Fe oxide-
163 hydroxide (FeA), crystalline Fe oxide-hydroxide, mainly goethite and hematite (FeD), and Fe associated with magnetite (FeM).

164 To extract FeA, samples were leached in an ascorbate solution buffered at pH 7.5 (Raiswell et al., 2008; Shi et al., 2011b). The
165 ascorbate solution contained a deoxygenated solution of 50 g L^{-1} sodium citrate, 50 g L^{-1} sodium bicarbonate, and 10 g L^{-1}
166 ascorbic acid. Around 30 mg of CFA was leached for 24 hours in 10 mL of ascorbate extractant, mixed continuously on a
167 rotary mixer. The extraction solution was then filtered through a $0.2 \mu\text{m}$ membrane filter. In order to extract FeD, the residue
168 was leached for 2 more hours in a dithionite solution buffered at pH 4.8 (50 g L^{-1} sodium dithionite in 0.35 M acetic acid and
169 0.2 M sodium citrate) (Raiswell et al., 2008; Shi et al., 2011b).

170 For the extraction of FeM, the CFA samples were first leached for 2 hours using a citrate-buffered dithionite solution to remove
171 FeD. The residue collected after filtration was then leached for 6 hours in a solution of 0.2 M ammonium oxalate ($(\text{NH}_4)_2\text{C}_2\text{O}_4$)
172 and 0.17 M $\text{H}_2\text{C}_2\text{O}_4$ at pH 3.2 (Poulton and Canfield, 2005). The Fe extractions were all carried out in the dark at room
173 temperature. The Fe concentration in the filtered extraction solutions was measured using the ferrozine method (Viollier et al.,
174 2000) or by inductively coupled plasma optical emission spectrometry (ICP-OES) analysis for the solutions containing high
175 concentration of oxalate.

176 The total Fe content in the samples was determined by microwave digestion in concentrated nitric acid (HNO_3) followed by
177 inductively coupled plasma mass spectrometry (ICP-MS) analysis.

178 The RSD% obtained for each extract using the Arizona test dust was 3% for FeA, 11% for FeD, 12% for FeM and 2% for the
179 total Fe ($n=7$).

180 2.4 X-ray absorption near edge structure (XANES) analysis

181 We collected XANES spectra to qualitatively examine the Fe speciation in the CFA samples. The XANES spectra at the Fe
182 K-edge were collected at the Diamond Light Source beamline I18. A Si(111) double-crystal monochromator was used in the
183 experiments. The beam size was $400 \mu\text{m} \times 400 \mu\text{m}$. The XANES spectra were collected from 7000 to 7300 eV at a resolution
184 varying from 0.2 eV for 3 s in proximity to the Fe K-edge (7100–7125 eV) to 5 eV for 1 s from 7100 to 7300 eV. Powder
185 samples were suspended in methanol and deposited on Kapton[®] tape. The analysis was repeated three times. We measured the
186 XANES spectra of the CFA-PM₁₀ fractions and mineral standards including hematite, magnetite, and illite. Data were
187 processed using the Athena program, part of the software package Demeter (version 0.9.26) (Ravel and Newville, 2005).



188 2.5 Model description

189 This study used the Integrated Massively Parallel Atmospheric Chemical Transport (IMPACT) model (Ito et al., 2021a and
190 references therein). The model simulates the emission, chemistry, transport, and deposition of Fe-containing aerosols and the
191 precursor gases of inorganic and organic acids. The coating of acidic species on the surface of Fe-containing aerosols promotes
192 the release of soluble Fe in the aerosol deliquescent layer and enhances the aerosol Fe solubility (Li et al., 2017). On the other
193 hand, the external mixing of oxalate-rich aerosols with Fe-rich aerosols can suppress the oxalate-promoted Fe dissolution at
194 low concentration of oxalate near the source regions (Ito, 2015). However, the internal mixing of alkaline minerals such as
195 calcium carbonate with Fe-containing dust aerosols can suppress the Fe dissolution (Ito and Feng, 2010). Since CFA particles
196 are co-emitted with acidic species, the transformation of relatively insoluble Fe in coal combustion aerosols into dissolved Fe
197 is generally much faster than that for mineral dust aerosols during their atmospheric lifetime (Ito, 2015; Ito and Shi, 2016).
198 Additionally, the size of CFA particles is substantially smaller than that of mineral dust. Thus, we adopted an observationally
199 constrained parameter for the dry deposition scheme (Emerson et al., 2020) to improve the simulation of dry deposition velocity
200 of fine particles.

201 To improve the accuracy of our simulations of Fe-containing aerosols, we revised the on-line Fe dissolution schemes in the
202 original model (Ito et al., 2021a) in conjunction with the mineralogy-based emission rates and a more dynamic range of pH
203 estimates. To implement 3-step dissolution schemes, we used the mineral-specific emission inventory for anthropogenic Fe
204 emissions (Rathod et al., 2020). To apply the Fe dissolution schemes for high ionic strength in aerosols, we used the mean
205 activity coefficient for pH estimate (Pye et al., 2020). Moreover, the dissolution rate was assumed to be dependent of pH for
206 highly acidic solutions ($\text{pH} < 2$) unlike in the former dissolution scheme (Ito, 2015), which allowed us to predict the sensitivity
207 of Fe dissolution to pH lower than 2.

208 To validate the new dissolution scheme, we compared our model results with observations of surface concentration of dissolved
209 Fe in $\text{PM}_{2.5}$ aerosol particles over the Bay of Bengal (Bikina et al., 2020).

210 3 Experimental results

211 3.1 Fe dissolution kinetics

212 We determined that Krakow ash had the largest buffer capacity, around 0.008 moles of buffered H^+ per litre, which was related
213 to the content of alkaline minerals in the sample. The buffer capacity of Aberthaw and Shandong ash was ~ 10 times smaller
214 than that of Krakow ash, around 0.0007 moles of buffered H^+ per litre. Leaching Krakow ash in 0.005 M H_2SO_4 , the initial
215 concentration of H^+ was similar to the concentration of the H^+ buffered. As a result, the solution pH raised from
216 approximately 2.1 to 2.7 corresponding to a pH change of around 20% (Table S1). For all the other experimental conditions,
217 the pH change was below 12% (Table S1). At the pH conditions used in this study (pH 1-3), acid buffering was fast and likely
218 occurred within the first 1-2 hours. We assumed that the calculated final pH was representative of the solution pH over the
219 duration of the experiments.

220 Dissolved Fe at different time intervals is reported as Fe%, which is the fraction of Fe dissolved to the total Fe content (FeT)
221 in the CFA samples. For all samples, a fast dissolution rate was observed at the beginning of the experiment. In the case of
222 Krakow ash, a dissolution plateau was reached after 2-hour leaching, which was likely due to the pH change. For that
223 sample/initial condition the pH increased to 2.7, and no more Fe was dissolved, leading to a total Fe solubility of $\sim 9\%$ over
224 the duration of the experiment (7 days) (Fig. 1a). Dissolving Krakow ash in 0.01 M H_2SO_4 (Fig. 1a), the experiment solution
225 had a final calculated pH of 2.1. The total Fe solubility was 34% at pH 2.1, almost 4 times higher than that at pH 2.7 (in 0.005
226 M H_2SO_4). Dissolution of Aberthaw and Shandong ash was slower compared to Krakow ash (Figs. 1b and 2c, respectively).



227 Leaching Aberthaw and Shandong ash in 0.005 M H₂SO₄ resulted in solutions with a pH of around 2.2. At this pH, the total
228 Fe solubility was 18% for Aberthaw ash and 21% for Shandong ash, which is 9-10 times higher than the total Fe solubility at
229 pH 2.9 (in 0.001 M H₂SO₄), around 2% for both samples.

230 The experimental treatment of dissolved Fe from Krakow ash in 0.05 H₂SO₄ solution with 1 M (NH₄)₂SO₄ (Fig. 1a) resulted
231 in a final predicted pH of 2.1. At that pH, the total Fe solubility of Krakow ash increased from 34% with no (NH₄)₂SO₄ to 48%
232 with high (NH₄)₂SO₄ concentration. The total Fe solubility of Krakow ash was around 28% at pH 3.0 with 1 M (NH₄)₂SO₄
233 (Fig. 1a), 3 times higher than that at pH 2.7 with no (NH₄)₂SO₄. At around pH 2, the total Fe solubility of Aberthaw (Fig. 1b)
234 and Shandong ash (Fig. 1c) increased by around 20% and 30% in the presence of (NH₄)₂SO₄. By contrast, the total Fe solubility
235 at pH 3.1 with 1 M (NH₄)₂SO₄ was 7.5% for Aberthaw ash (Fig. 1b) and 14% for Shandong ash (Fig. 1c), respectively, which
236 was around 4 and 7 times higher than in the experiments carried out at pH 2.9 without (NH₄)₂SO₄.

237 The Fe dissolution of the CFA samples in H₂SO₄ solutions with 0.01 M H₂C₂O₄ (at around pH 2) is shown in Fig. 2. The total
238 Fe solubility of Krakow ash at pH 1.9 with 0.01 M H₂C₂O₄ was 61% (Fig. 2a), which was almost 2 times higher than that at
239 pH 2.1 but without H₂C₂O₄ (Fig. 2a). For Aberthaw ash, oxalate contribution to the dissolution process led to a total Fe
240 solubility of 30% at pH 2.0 (Fig. 2b), which was 70% higher than in the experiment carried out in 0.005 M H₂SO₄ (~pH 2.2)
241 (Fig. 2b). Shandong ash dissolution behaviour was not affected by the presence of oxalate (Fig. 2c).

242 We also investigated the effect of high (NH₄)₂SO₄ concentration on oxalate-promoted dissolution. In Fig. 2a, the total Fe
243 solubility of Krakow ash decreased from 61% at pH 1.9 in the presence of oxalate to 54% at pH 2.0 with oxalate and (NH₄)₂SO₄.
244 For Aberthaw ash, the total Fe solubility at pH 2.0 decreased from 30% in the presence of oxalate to 19% after the addition of
245 (NH₄)₂SO₄ (Fig. 2b).

246 Figure 3 shows the Fe dissolution behaviour of Krakow ash at different pH conditions in the presence of 1 M (NH₄)₂SO₄ and
247 H₂C₂O₄ (0.01-0.03 M depending on the solution pH). The total concentration of oxalate ions was calculated using the E-AIM
248 model and was similar at different pH conditions, 0.015 at pH 1.0 (Experiment 7 Table S2), 0.009 at pH 2.0, and 0.01 at pH
249 2.9 (Experiments 3 Table S2). The highest total Fe solubility was observed at pH 1.0 (~67%). At pH 2.0, the total Fe solubility
250 decreased to 54%, and no substantial variations were observed between pH 2.0 and pH 2.9 (54%-51%). At pH 1.0, the
251 concentration of H⁺ was considerably higher compared to pH 2.0-2.9, leading to a faster dissolution rate. The total
252 concentration of oxalate ions was 1.5-1.6 times higher in the solution at pH 1.0 than at pH 2.0-2.9, which may also contribute
253 to the faster dissolution rate. C₂O₄²⁻ concentration increased with rising pH. Although the concentration of H⁺ was lower at pH
254 2.9 than at pH 2.0, the E-AIM model estimated that C₂O₄²⁻ contributed around 35% of the total oxalate concentration at pH
255 2.9, which was 4.5 times higher than at pH 2.0 (Experiments 3 Table S2). The similar dissolution behaviour at pH 2.0 and pH
256 2.9 conditions may reflect the combination of these two opposite factors, higher concentration of C₂O₄²⁻ but lower
257 concentration of H⁺ at pH 2.9 compared to 2.0.

258 We determined the Fe dissolution behaviour of Krakow ash at pH 1.0 in the presence of oxalate and increasing concentrations
259 of (NH₄)₂SO₄. The ash was leached in H₂SO₄ solutions with 0.03 M H₂C₂O₄ at pH 1.0, while the concentration of (NH₄)₂SO₄
260 varied from 0 to 1.5 M. In Fig. 4, the total Fe solubility of Krakow ash in the presence of oxalate was 75% at pH 1.0 and
261 decreased to 68% after the addition of 0.5 M (NH₄)₂SO₄. Higher (NH₄)₂SO₄ concentrations did not affect the Fe dissolution
262 behaviour in the presence of oxalate at pH 1.0.

263 3.2 Fe speciation

264 The Fe phases in the CFA samples determined through sequential extractions are shown in Fig. 5. The Fe speciation in the
265 Saharan dust sample is added for comparison. Krakow ash had a total Fe (FeT) content of 5.2%, while FeT in Aberthaw and



266 Shandong ash was 3.1% and 1.6% respectively. Amorphous Fe (FeA/FeT) was 6.5% in Krakow ash, 2% in Aberthaw ash, and
267 4.6% in Shandong ash. The CFA samples showed very different dithionite Fe (FeD/FeT) content, 21.5% in Krakow ash, 8%
268 in Aberthaw ash and 14.8% in Shandong ash. The content of magnetite (FeM/FeT) was considerably higher in Krakow ash
269 (22.4%) compared to Aberthaw (2.9%) and Shandong (4.5%) ash. About 50 %–87 % of Fe was contained in other phases most
270 likely in aluminosilicates. Overall, CFA had more magnetite and highly reactive amorphous Fe and less dithionite Fe than
271 Libya dust.

272 In Fig. S2, the Fe K-edge XANES spectra of Krakow and Aberthaw ash showed a single peak in the pre-edge region at around
273 7114.3 eV and 7114.6 eV, respectively. In the edge region, Aberthaw ash showed a broad peak at around 7132.2 eV, while the
274 peak of Krakow ash was slightly shifted to 7132.9 eV and narrower. The pre-edge peak at around 7115.4 suggest that Fe was
275 mainly as Fe(III). The spectral features of Aberthaw and Krakow ash are different from those of the hematite, magnetite and
276 illite standards suggesting that the glass fraction was dominant and controlled their spectral characteristics, which is consistent
277 with the results of the Fe sequential extractions. The XANES Fe K-edge spectra of the CFA samples have some common
278 features with those of Icelandic dust, but differs from northern African dust (Fig. S2). Aluminium silicate glass is also dominant
279 in Icelandic dust (Baldo et al., 2020). In the pre-edge region, Icelandic dust (sample MIR 45 in Fig. S2) showed a main peak
280 at around 7114.4 eV and a second less intense peak at around 7112.7 eV, while a broad peak was observed at around 7131.9
281 eV in the edge region (Baldo et al., 2020). Northern African dust (western Sahara in Fig. S2) showed a distinct double peak in
282 the pre-edge region at around 7113.9 and 7115.2 eV, and a main peak in the edge region at around 7133.3 eV (Baldo et al.,
283 2020).

284 4 Fe simulation from the IMPACT model

285 4.1 Fe dissolution scheme

286 Based on the laboratory experiments carried out on the CFA samples, we implemented a 3-step dissolution scheme for proton-
287 promoted and oxalate-promoted Fe dissolution (Table 1). The Fe dissolution kinetics was described as follows (Ito, 2015):

$$288 \sum_i RFe_i = k_i(pH, T) \times a(H^+)^{m_i} \times f_i \quad (1)$$

289 where RFe_i is the dissolution rate of individual mineral i , k_i is the rate constant (moles Fe $g^{-1} s^{-1}$), $a(H^+)$ is the H^+ activity in
290 solution, m_i represents the empirical reaction order for protons. The function f_i ($0 \leq f_i \leq 1$) accounts for the suppression of
291 mineral dissolution by competition for oxalate between surface Fe and dissolved Fe (Ito, 2015):

$$292 f_i = 0.17 \times \ln([\text{lig}] \times [Fe]^{-1})_i + 0.63 \quad (2)$$

293 in which, $[Fe]$ is the molar concentration (mol L^{-1}) of Fe^{3+} dissolved in solution, and $[\text{lig}]$ is the molar concentration of ligand
294 (e.g., oxalate). f_i was set to 1 for the proton-promoted dissolution.

295 The scheme assumes 3 rate constants “fast”, “intermediate” and “slow” for the proton-promoted, and the proton + oxalate-
296 promoted dissolution (Table 1). These were obtained by fitting the parameters to our measurements for Krakow ash in H_2SO_4
297 and $(NH_4)_2SO_4$ at pH 2-3, with and without oxalate (Experiments 2 and 3 in Table S1), which are shown in Fig. 6. The fast
298 rate constant represents highly reactive Fe species such as amorphous Fe oxyhydroxides, Fe carbonates and Fe sulphates. The
299 intermediate rate constant can be applied to nano-particulate Fe oxides, while more stable phases including for example Fe-
300 aluminosilicate and crystalline Fe oxides have generally slower rate (Ito and Shi, 2016; Shi et al., 2011a; Shi et al., 2011b; Shi
301 et al., 2015). Similarly, we predicted the dissolution kinetics of Aberthaw ash and Shandong ash (Figs. S3-S5). The dissolution



302 kinetic of Krakow ash was calculated based also on the experimental results at pH 1.0, which is shown in Fig. S6 in comparison
303 with kinetics predicted at pH 2.0 and pH 2.9 conditions.

304 The contribution of the oxalate-promoted dissolution to dissolved Fe was derived as the difference between the estimated
305 dissolution rates for the proton + oxalate-promoted dissolution and the proton-promoted dissolution:

$$306 \quad R_{\text{Fe}_i(\text{oxalate})} = R_{\text{Fe}_i(\text{proton} + \text{oxalate})} - R_{\text{Fe}_i(\text{proton})} \quad (3)$$

307 The Fe dissolution rates were predicted at a wider range of pH using Eq. (1) and Eq. (3) and the parameters in Table 1:

$$308 \quad R_{\text{Fe}_i} = R_{\text{Fe}_i(\text{proton} + \text{oxalate})} \text{ when } R_{\text{Fe}_i(\text{oxalate})} < 0 \quad (4)$$

309 Since $R_{\text{Fe}_i(\text{oxalate})}$ is less than 0 at low pH (< 2), this equation applies to highly acidic conditions. As a result, the predicted
310 amount of dissolved Fe was smaller when using the dissolution rate for the proton + oxalate-promoted dissolution, $R_{\text{Fe}_i(\text{proton} +$
311 $\text{oxalate})}$, rather than the rate for the proton-promoted dissolution, $R_{\text{Fe}_i(\text{proton})}$, at pH < 2 . Accordingly, the dissolution rate, R_{Fe_i} ,
312 was less dependent on the pH compared to $R_{\text{Fe}_i(\text{proton})}$ at highly acidic conditions, possibly due to the competition for the
313 formation of surface complexes.

314 At pH > 2 when oxalate does promote Fe dissolution, the following equation applies:

$$315 \quad R_{\text{Fe}_i} = R_{\text{Fe}_i(\text{proton})} + R_{\text{Fe}_i(\text{oxalate})} \text{ when } R_{\text{Fe}_i(\text{oxalate})} > 0 \quad (5)$$

316 **4.2 Surface concentration of dissolved Fe over the Bay of Bengal**

317 The new dissolution scheme was applied in the IMPACT atmospheric chemistry transport model to predict the surface
318 concentration of dissolved Fe in atmospheric particles collected over the Bay of Bengal, which is an area for which there are
319 detailed field measurements available (Bikkina et al., 2020; Kumar et al., 2010; Srinivas and Sarin, 2013; Srinivas et al., 2012)
320 and multi-modelling analyses have been done (Ito et al., 2019). It thus represents a test for our experimental results in actual
321 field conditions. Three sensitivity simulations were performed to explore the effects of the uncertainties associated with the
322 dissolution schemes and mineralogical component of Fe. In addition, the former setting (Ito et al., 2021a) was used in the
323 IMPACT model for comparison.

324 In sensitivity Test 0, the total Fe emission in anthropogenic aerosols was estimated using Fe emission factors by each sector
325 such as energy, heavy industry, and iron and steel industry for the simulation years (Ito et al., 2018), whereas in sensitivity
326 Test 1, Test 2, and Test 3, the mineral specific emission inventory for the year 2010 by Rathod et al. (2020) was used. In Test
327 0, we ran the model without the upgrades of the dissolution scheme discussed in section 2.4, and apply in addition the
328 photoinduced dissolution scheme for both combustion and dust aerosols (Ito, 2015; Ito and Shi, 2016), which was turned off
329 in Test 1, Test 2, and Test 3 due to the lack of laboratory measurements under high ionic strength. To estimate the aerosol pH,
330 we applied a H^+ activity coefficient of 1 for Test 0, while the mean activity coefficient from Pye et al. (2020) was used for the
331 other tests. The dissolution rate was assumed as pH-independent for highly acidic solutions (pH < 2) (Ito, 2015) in Test 0,
332 based on the laboratory measurements in Chen et al. (2012), while no pH threshold was considered in Test 1, Test 2, and Test
333 3 as the total dissolution (proton + oxalate) was suppressed at pH < 2 from the predicted dissolution rate.

334 In Test 1, we used the new dissolution scheme accounting for the proton- and oxalate- promoted dissolution of Krakow ash
335 for all combustion aerosols in the model (Table 1). The dissolution kinetics was calculated using the mineral-specific inventory
336 for anthropogenic Fe emissions (Rathod et al., 2020). The Fe composition of wood was used for open biomass burning (Matsuo
337 et al., 1992). In this simulation, 3 Fe pools were considered. Sulphate Fe in Rathod et al. (2020) was assumed as fast pool,



338 magnetite Fe as intermediate pool, hematite and Fe-aluminosilicate as slow pool. In Test 2, we calculated the dissolution
339 kinetics only considering the proton-promoted dissolution. In Test 3, the Fe pools were as determined here for Krakow ash:
340 ascorbate Fe (FeA) as fast pool, magnetite Fe (FeM) as intermediate pool, hematite plus goethite Fe (FeD) and other Fe as
341 slow pool (Fig. 5). FeA contains highly reactive Fe species with fast dissolution rates (Raiswell et al., 2008; Shi et al., 2011b).
342 FeM appeared to work well for the different fly ash samples in the dissolution scheme as intermediate Fe pool. FeD is
343 associated with crystalline Fe oxides and a predominant proportion of this is highly insoluble (Raiswell et al., 2008; Shi et al.,
344 2011b), thus it was considered as slow pool in the dissolution scheme. We assumed other Fe to be mostly as Fe-bearing
345 aluminosilicates and considered this as slow Fe pool.

346 The temporally and regionally averaged, model-calculated surface concentration of aerosol Fe (Fig. 7), dissolved Fe (Fig. 8)
347 and Fe solubility (Figs. 9 and S7) for the fine mode (PM_{2.5}) along the cruise tracks were compared with the measurements over
348 the Bay of Bengal for the period extending from 27 December 2008 to 26 January 2009 (Bikkina et al., 2020). The average
349 aerosol Fe concentration observed over the Bay of Bengal varies from $145 \pm 144 \text{ ng m}^{-3}$ over the North Bay of Bengal (27
350 December 2008 - 10 January 2009) to $55 \pm 23 \text{ ng m}^{-3}$ over the South Bay of Bengal (11-26 January 2009) (Bikkina et al.,
351 2020). In Fig. 7, the modelled aerosol Fe concentrations exhibit a similar variability to that of measurements with relatively
352 higher values over the North Bay of Bengal ($101 \pm 57 \text{ ng m}^{-3}$ in Test 0, and $81 \pm 37 \text{ ng m}^{-3}$ in Test 1-3) compared to the South
353 Bay of Bengal ($21 \pm 13 \text{ ng m}^{-3}$ in Test 0, and $34 \pm 25 \text{ ng m}^{-3}$ in Test 1-3). The model reproduced the source apportionment of Fe
354 (Fig. 7) which is qualitatively derived from previous observational studies indicating that the aerosol Fe concentrations over
355 the North Bay of Bengal are influenced by emissions of dust and combustion sources from the Indo-Gangetic Plain (Kumar et
356 al., 2010), whereas combustion sources (e.g., biomass burning and fossil-fuel) from South-East Asia are dominant over the
357 South Bay of Bengal (Kumar et al., 2010; Srinivas and Sarin, 2013). On the other hand, the model could not reproduce the
358 peak in total Fe concentration (1.8% of Fe content in PM_{2.5} sample) reported around 29 December 2008. The total Fe observed
359 in PM_{2.5} (613 ng m^{-3}) is higher than that in PM₁₀ (430 ng m^{-3}) (Srinivas et al., 2012). This may be due to the measurement
360 uncertainty including sample collection with two different high-volume samplers (Kumar et al., 2010).

361 The average aerosol dissolved Fe concentration measured over the North Bay of Bengal ($16 \pm 9 \text{ ng m}^{-3}$) is slightly lower than
362 that over the South Bay of Bengal ($18 \pm 10 \text{ ng m}^{-3}$) (Bikkina et al., 2020). The model prediction of dissolved Fe over the North
363 Bay of Bengal was $6 \pm 2 \text{ ng m}^{-3}$ Fe in Test 0, $21 \pm 10 \text{ ng m}^{-3}$ in Test 1, and $31 \pm 28 \text{ ng m}^{-3}$ in Test 2, and $13 \pm 10 \text{ ng m}^{-3}$ in
364 Test 3. The aerosol dissolved Fe estimated over the South Bay of Bengal was $6 \pm 1 \text{ ng m}^{-3}$ in Test 0, $15 \pm 10 \text{ ng m}^{-3}$ in Test 1,
365 $32 \pm 22 \text{ ng m}^{-3}$ in Test 2, and $12 \pm 7 \text{ ng m}^{-3}$ in Test 3. In Fig. 8, our model results show that the contribution of mineral dust
366 to aerosol dissolved Fe was higher over the North Bay of Bengal ($14\% \pm 6\%$ in Test 1, $28\% \pm 34\%$ in Test 2, and $33\% \pm 26\%$
367 in Test 3) compared to the South Bay of Bengal ($3\% \pm 1\%$ in Test 1, $1\% \pm 1\%$ in Test 2, and $3\% \pm 1\%$ in Test 3). Overall,
368 anthropogenic combustion sources were dominant over the Bay of Bengal accounting for $84\% \pm 12\%$ in Test 1, $72\% \pm 29\%$
369 in Test 2, and $69\% \pm 24\%$ in Test 3 of the aerosol dissolved Fe. Moreover, after 22 January 2009, the contribution of open
370 biomass burning sources increased up to 47% in Test 1, 64% in Test 2, and 60% in Test 3 (Fig. 8).

371 The aerosol Fe solubility measured over the South Bay of Bengal is higher than that over the North Bay of Bengal, respectively
372 $32\% \pm 11\%$ and $15\% \pm 7\%$ (Bikkina et al., 2020), and model estimates showed a similar trend (Fig. S7). In Fig. S7, the
373 calculated average Fe solubility over the North Bay of Bengal in Test 3 ($18\% \pm 10\%$) was in good agreement with observations,
374 while lower Fe solubility was estimated in Test 0 ($8\% \pm 5\%$) and higher values were obtained for Test 1 ($28\% \pm 8\%$). The
375 aerosol Fe solubility over the South Bay of Bengal was better captured in Test 1 ($43\% \pm 4\%$) and Test 3 ($39\% \pm 7\%$), whereas
376 Test 0 showed higher variability ($38\% \pm 22\%$). The proton-promoted dissolution scheme in Test 2 significantly overestimated
377 the Fe solubility over the Bay of Bengal (Figs. 9 and S7). The aerosol Fe solubility was largely overestimated in all scenarios
378 after 22 January 2009, as open biomass burning sources become dominant (Fig. 8). The comparison between observations and



379 model predictions of Fe solubility over the Bay of Bengal is shown in Fig. 9. The agreement between measurements and model
380 predictions was the best in Test 1 and Test 3. These exhibited good correlation with observations ($R = 0.60$ in Test 1 and $R =$
381 0.51 in Test 3), and the lowest centred root-mean-square (RMS) difference between the simulated and observed aerosol Fe
382 solubilities ($RMS = 16$ in Test 1 and $RMS = 14$ in Test 3). In Test 0, the model estimates showed higher difference from
383 observations ($RMS = 22$) and poor correlation ($R = 0.30$).

384 5 Discussion

385 5.1 Dissolution behaviour of Fe in CFA

386 In this study, the Fe dissolution kinetics of CFA samples from UK, Poland and China was investigated under simulated
387 atmospheric acidic conditions. A key parameter in both the atmosphere and the simulation experiments is the pH of the water
388 interacting with the CFA particles. The lower the pH of the experimental solution the faster the dissolution and eventually the
389 higher the amount of Fe dissolved. Our results showed a strong pH dependence in low ionic strength conditions, with higher
390 dissolution rate at lower pH. For example, reducing the solution pH from 2.7 to 2.1, the Fe solubility of Krakow ash increased
391 by a factor of 4 (Fig. 1a) over the duration of the experiments, while the Fe solubility of Aberthaw and Shandong ash increased
392 by 9-10 times from pH 2.9 to pH 2.2 (Figs. 1b-c). This enhancement is higher than that observed in studies conducted on
393 mineral dust samples, which showed that one pH unit can lead to 3-4 times difference in dissolution rates (Ito and Shi, 2016;
394 Shi et al., 2011a). Furthermore, Chen et al. (2012) reported that the Fe solubility of the certified CFA 2689 only increased by
395 10% from pH 2 to pH 1, after 50 hours of dissolution in acidic media. The Fe solubility of CFA (PM₁₀ fractions) after 6 hours
396 at pH 2 was 6%-10% for Aberthaw and Shandong ash respectively, and 28% for Krakow ash (Fig. 1). These values are higher
397 than the Fe solubilities measured by Fu et al. (2012), who reported 2.9%-4.2% Fe solubility in bulk CFA from three coal-fired
398 power plants in China after 12-hour leaching at pH 2. This suggest that Fe in our CFA samples initially dissolved faster than
399 those used in Fu et al. (2012). The Fe solubility after 72-hour leaching in H₂SO₄ at around pH 2 varied from around 12% and
400 17% (Aberthaw and Shandong ash) to 34% (Krakow ash). These values are at the lower end of the range or below those
401 reported in Chen et al. (2012), who measured a Fe solubility of ~20%-70% in certified CFA samples after accumulated acid
402 dissolution of 72 hours at pH 2. These results suggest that there are considerable variabilities in the pH dependent dissolution
403 of Fe in CFA.

404 Our results showed that high ionic strength has a major impact on dissolution rates of CFA at low pH (i.e., pH 2-3). The Fe
405 solubility of CFA increased by approximately 20%-40% in the presence of 1 M (NH₄)₂SO₄ at around pH 2 over the duration
406 of the experiments, and by a factor from 3 to 7 at around pH 3 conditions (Fig. 1). At high ionic strength, the activity of ions
407 in solution is reduced, thus, in order to maintain similar pH conditions, the H⁺ concentration has to be increased (Table S1).
408 Although Fe dissolution was primarily controlled by the concentration of H⁺, the high concentration of sulphate ions could be
409 also an important factor contributing to Fe dissolution, in particular when the concentration of H⁺ in the system was low (e.g.,
410 pH 3). Previous research found that the high ability of anions to form soluble complexes with metals can enhance Fe dissolution
411 (Cornell et al., 1976; Cornell and Schwertmann, 2003; Furrer and Stumm, 1986; Hamer et al., 2003; Rubasinghege et al., 2010;
412 Sidhu et al., 1981; Surana and Warren, 1969). Sulphate ions adsorbed on the particles surface form complexes with Fe (e.g.,
413 Rubasinghege et al., 2010). This may increase the surface negative charge favouring the absorption of H⁺ and thereby increase
414 the dissolution rate. In addition, the formation of surface complexes may weaken the bonds between Fe and the neighbouring
415 ions (Cornell et al., 1976; Furrer and Stumm, 1986; Sidhu et al., 1981). Cwierny et al. (2008) reported that at pH 1-2 the high
416 ionic strength generated by NaCl up to 1 M did not influence Fe dissolution of mineral dust particles. However, Ito and Shi
417 (2016) showed that the high ionic strength resulting from the addition of 1 M (NH₄)₂SO₄ in leaching solutions at pH 2-3
418 enhanced the Fe dissolution of dust particles, which was also observed here for the CFA samples. Borgatta et al. (2016)



419 compared the Fe solubility of CFA from USA Midwest, North-East India, and Europe in acidic solution (pH 1-2) containing
420 1 M NaCl. The Fe solubility measured after 24 hours varied from 15% to 70% in different CFA (bulk samples) at pH 2 with 1
421 M NaCl, which was considerably higher than that observed at pH 2 with 1 M NaNO₃ (<20%) (Kim et al., 2020). Both studies
422 did not investigate the impact of ionic strength on the dissolution behaviour, i.e., by comparing the dissolution at low and high
423 ionic strength. Note that both studies did not specify how the pH conditions were maintained at pH 2. Here, we considered the
424 most important sources of high ionic strength in aerosol water and simulated Fe dissolution in the presence of (NH₄)₂SO₄ and
425 H₂C₂O₄ under acidic conditions. We emphasize that the pH under high ionic strength here is estimated from a thermodynamic
426 model, similar to those implemented in the IMPACT model.

427 The presence of oxalate enhanced Fe dissolution in Krakow and Aberthaw ash but not in Shandong ash at around pH 2 (Fig.
428 2). The effect of oxalate on the Fe dissolution kinetics has also been studied by Chen and Grassian (2013) at pH 2 (11.6 mM
429 H₂C₂O₄). After 45-hour leaching, the Fe solubility of the certified CFA 2689 increased from 16% in H₂SO₄ at pH 2 to 44% in
430 H₂C₂O₄ at the same pH (Chen and Grassian, 2013). Therefore, the enhancement in Fe solubility of CFA in the presence of
431 oxalate observed in this study (from no impact in Shandong ash to doubled dissolution in Krakow ash) is lower than that
432 reported for the certified CFA 2689 which was around by 2.8 times (Chen and Grassian, 2013). Since no data are available in
433 Chen and Grassian (2013), we are unable to make a comparison with the other two certified CFA samples. The Fe solubility
434 of Krakow ash after 48-hour leaching at pH 1.9 with 0.01 M H₂C₂O₄ (Fig. 2a) was 53%, which is within the range observed
435 in Chen and Grassian (2013) for the certified CFA samples at similar pH and H₂C₂O₄ concentrations (from 44% to 78%),
436 whereas the Fe solubility of Aberthaw and Shandong ash (Figs. 2b-c, 18%-17% after 48-hour leaching at pH 2.0 with 0.01 M
437 H₂C₂O₄) was considerably lower than that of certified CFA (Chen and Grassian, 2013). These results suggest a large variability
438 in the effects of oxalate on the Fe dissolution rates in different types of CFA.

439 Our results also indicated that high (NH₄)₂SO₄ concentrations suppress oxalate-promoted Fe dissolution of CFA (Fig. 2), which
440 was not considered in previous research. At pH 1.9 in the presence of oxalate, the Fe solubility of Krakow ash decreased by
441 around 10% after the addition of (NH₄)₂SO₄, while the Fe solubility of Aberthaw ash decreased by 35% (Fig. 2). We used the
442 E-AIM model to estimate the concentration of oxalate ions and their activity (Table S2). The pH influences the speciation of
443 H₂C₂O₄ in solution (e.g., Lee et al., 2007). H₂C₂O₄ is the main species below pH 2, whereas HC₂O₄⁻ is dominant between pH
444 1-4. Above pH 4, C₂O₄²⁻ is the principal species. In our experiments, H₂C₂O₄ is mainly as HC₂O₄⁻ at around pH 2 (Experiments
445 3-4 in Table S2). In the presence of (NH₄)₂SO₄, the activity coefficient of HC₂O₄⁻ was reduced by approximately 35-38%
446 (Experiments 3 in Table S2). Increasing the ionic strength lowers the activity of the oxalate ions, but at the same time favours
447 the dissociation of the acid. At around pH 2 conditions, the E-AIM model estimated that the activity of C₂O₄²⁻ was reduced by
448 around one order of magnitude in the presence of (NH₄)₂SO₄, while its concentration increased 12-15 times (Experiments 3 in
449 Table S2). The adsorption of anions can reduce oxalate adsorption on the particle surface due to electrostatic repulsion which
450 results in slower dissolution rates (Eick et al., 1999). Precipitation of ammonium hydrogen oxalate (NH₄HC₂O₄) can also occur
451 in the system, but this is very soluble and easily re-dissolves forming soluble oxalate species (Lee et al., 2007). We speculate
452 that the high concentration of sulphate ions is likely to be responsible for inhibiting the oxalate-promoted dissolution by
453 reducing oxalate adsorption on the particle surface. At pH 1 in the presence of oxalate, increasing the concentration of
454 (NH₄)₂SO₄ from 0.5 M to 1.5 M did not affect the Fe dissolution behaviour of the CFA samples (Fig. 4). As previously
455 discussed, the adsorption of sulphate ions on the particle surface may inhibit oxalate-promoted dissolution. However, once the
456 saturation coverage is reached, increasing the concentration of anions has no further effect on the dissolution rate (Cornell et
457 al., 1976).

458 Fe speciation is an important factor affecting the Fe dissolution behaviour. CFA particles have very different chemical and
459 physical properties depending for example on the nature of coal burned, combustion conditions, cooling process and particle



460 control devices implemented at the power stations (e.g., Blissett and Rowson, 2012; Yao et al., 2015). This is likely the reason
461 why the Fe speciation observed in the CFA samples analysed in this study from different location varied considerably (Fig. 5).
462 In the CFA samples, the Fe dissolution curves for different pH and ionic strengths generally showed the greatest rate of Fe
463 release within the first 2 hours, followed by a slower dissolution, reaching almost a plateau at the end of the experimental run.
464 This indicates the presence of multiple Fe phases in CFA particles with a wide range of reactivity. Initially, highly reactive
465 phases were the main contribution to dissolved Fe. As the dissolution continued, more stable phases became the dominant
466 source of dissolved Fe (Shi et al., 2011a). SEM analysis conducted on CFA samples showed that CFA particles are mostly
467 spherical (e.g., Chen et al., 2012; Dudas and Warren, 1987; Valeev et al., 2018; Warren and Dudas, 1989) with Fe oxide
468 aggregates on the surface (Chen et al., 2012; Valeev et al., 2018). The analysis of the CFA samples processed in aqueous
469 solution at low pH suggests that initially Fe dissolved from the reactive external glass coating (Dudas and Warren, 1987;
470 Warren and Dudas, 1989) and from the Fe oxide aggregates on the particle surface (Chen et al., 2012; Valeev et al., 2018).
471 Subsequently, Fe is likely realised from the structure of the aluminium silicate glass (Chen et al., 2012; Dudas and Warren,
472 1987; Valeev et al., 2018; Warren and Dudas, 1989), and crystalline Fe oxide phases (Warren and Dudas, 1989). Overall,
473 Krakow ash showed the fastest dissolution rates, but the dissolution of highly reactive Fe species as FeA is insufficient to
474 account for the high Fe solubility observed at low pH. Our results showed that once the FeA dissolved, additional Fe was
475 dissolved from more refractory Fe phases. The modelled dissolution kinetics obtained using FeM as intermediate pool were in
476 good agreements with measurements (Figs. S3-S6). FeM is likely to be primary magnetite but may contain a fraction of the
477 more reactive aluminosilicate glass. Our model results suggest that magnetite in CFA particles may be more soluble than has
478 been shown in Marcotte et al. (2020). It is possible that in real CFA samples the mineral physicochemical properties including
479 for example crystal size, degree of crystallinity, cationic and anionic substitution in the lattice which influence the Fe
480 dissolution behaviour (e.g., Schwertmann, 1991) are likely to be different from those of the reference minerals analysed in
481 Marcotte et al. (2020). In order to estimate in detail the relative contribution of different mineral phases to dissolved Fe, most
482 detailed work would be needed to determine Fe mineral phases in pristine and processed CFA particles.

483 Finally, the modelled dissolution kinetics obtained using the new dissolution scheme for CFA (Table 1) showed better
484 agreement with laboratory measurements than when using the original scheme (Ito, 2015) (Figs. S8 and S9). In Fig. S8, we
485 compared the Fe dissolution kinetics of Krakow ash at around pH 2 and 3 with 1 M $(\text{NH}_4)_2\text{SO}_4$ calculated using the proton-
486 promoted dissolution scheme in Table 1 with the dissolution kinetics calculated at similar pH but using the proton-promoted
487 dissolution scheme for combustion aerosols in Ito (2015) (Table S3). The dissolution scheme in Ito (2015) was based on
488 laboratory measurements conducted at low ionic strength (Chen et al., 2012) and assumed a single Fe phase in combustion
489 aerosol particles, while the new dissolution scheme considered the high ionic strength of aerosol water and assumed three rate
490 constants, for fast, intermediate and slow kinetics of the different Fe phases present in CFA particles. The Fe dissolution
491 kinetics obtained using the new dissolution scheme showed a better agreement with measurements and was enhanced compared
492 to the model estimates obtained using the original dissolution scheme (Ito, 2015) for low ionic strength conditions (Fig. S8).
493 Figure S9 shows the Fe dissolution kinetics of Krakow ash at pH 2.0 and 2.9 with 0.01 M $\text{H}_2\text{C}_2\text{O}_4$ and 1 M $(\text{NH}_4)_2\text{SO}_4$
494 calculated using the proton- and oxalate-promoted dissolution scheme in Table 1 and the dissolution kinetics calculated at
495 similar pH and $\text{H}_2\text{C}_2\text{O}_4$ concentration but using the scheme in Ito (2015) (i.e., single phase dissolution, see Table S3). The Fe
496 dissolution kinetics predicted using the new dissolution scheme had a much better agreement with measurements. Figure S9c
497 shows the suppression of the oxalate-promoted dissolution at pH 2.0 and high $(\text{NH}_4)_2\text{SO}_4$ concentrations. At pH 2, the proton-
498 promoted dissolution was comparable to the proton + oxalate-promoted dissolution (Fig. S9c), with $R\text{Fe}_{(\text{oxalate})}$ close to zero
499 (see Eq. 3). At pH 2.9, the proton + oxalate-promoted dissolution was higher than the proton + oxalate-promoted dissolution
500 (Fig. S9d), with $R\text{Fe}_{(\text{oxalate})} > 0$ (Eq. 5).



501 Moreover, the new 3-step dissolution scheme better captured the initial fast dissolution of CFA (Figs. 2-3) which was also
502 observed in previous research (Borgatta et al., 2016; Chen et al., 2012; Chen and Grassian, 2013; Fu et al., 2012; Kim et al.,
503 2020) (except for the certified CFA 2689 in Chen et al. (2012) which showed increasing dissolution rates over the duration of
504 the experiment). Furthermore, the new scheme enabled us to account for the different Fe speciation determined in the CFA
505 samples, which could be a key factor contributing to the different Fe dissolution behaviour observed in the present study and
506 in literature (Borgatta et al., 2016; Chen et al., 2012; Chen and Grassian, 2013; Fu et al., 2012; Kim et al., 2020). In Figs. S3-
507 S5, the dissolution kinetics of Aberthaw and Shandong ash calculated using the dissolution rates in Table 1 and the Fe phases
508 determined in the samples showed a good agreement with measurements.

509 **5.2 Comparison with mineral dust**

510 High ionic strength also impacted the dissolution rates of the Saharan dust sample at low pH (Fig. S10). At around pH 2
511 conditions, the proton-promoted Fe dissolution of Libya dust was enhanced by ~40% after the addition of $(\text{NH}_4)_2\text{SO}_4$. At
512 around pH 2 and with 0.01 M $\text{H}_2\text{C}_2\text{O}_4$, the Fe solubility of Libya dust decreased by ~30% in the presence of $(\text{NH}_4)_2\text{SO}_4$.
513 Overall, the Fe solubility of Libya dust was lower compared to that observed in the CFA samples. After 168 hour-leaching at
514 pH 2.1 with 1 M $(\text{NH}_4)_2\text{SO}_4$, the Fe solubility of Libya dust was 7.2% (Fig. S10), which was from around 3 to 7 times lower
515 compared to that of the CFA samples (Fig. 1). At around pH 2 conditions in the presence of oxalate and high $(\text{NH}_4)_2\text{SO}_4$
516 concentration, the Fe solubility of Libya dust rose to ~13.6% (Fig. S10), which is still 4 times lower than that of Krakow ash
517 and around 1.5 lower than Aberthaw and Shandong ash (Fig. 2). The Fe solubilities of Libya dust observed in this study are
518 comparable with those of the Tibesti dust in Ito and Shi (2016) at similar experimental conditions.

519 The enhanced Fe solubility in CFA compared to mineral dust could be primarily related to the different Fe speciation (Figs. 5
520 and S2). CFA contained more highly reactive Fe and magnetite but less hematite and goethite than mineral dust.

521 Although mineral dust is the largest contribution to aerosol Fe while CFA accounts for only a few percent, atmospheric
522 processing of CFA may result in a larger than expected contribution of bioavailable Fe deposited to the surface ocean. It is
523 thus important to quantify the amount and nature of CFA in atmospheric particles.

524 **5.3 Comparison of modelled Fe solubility with field measurements**

525 The model results obtained using the emission inventory from Rathod et al. (2020) and the new dissolution scheme for the
526 proton + oxalate-promoted dissolution (Table 1) in Test 1 and Test 3 provided a better estimate of dissolved Fe over the Bay
527 of Bengal than the other tests (Figs. 8, 9, and S7). At the same time, the new model improved the agreement of aerosol Fe
528 solubility from Test 0 ($70\% \pm 4\%$) to Test 1 ($44\% \pm 3\%$) and Test 3 ($48\% \pm 1\%$) with the field data ($25\% \pm 3\%$) but still
529 overestimated it after 22 January 2009, when open biomass burning sources become dominant (Fig. 8). This could be due to
530 the unrepresentative Fe speciation used in Test 1 and Test 3 for biomass burning over the Bay of Bengal. To reduce the
531 uncertainty in model predictions, emission inventories could be improved through a comprehensive characterization of Fe
532 species in combustion aerosol particles.

533 The revised model also enabled us to predict sensitivity to a more dynamic range of pH changes, particularly between
534 anthropogenic combustion and biomass burning. The results show that the proton-promoted dissolution scheme in Test 2
535 significantly overestimated aerosol dissolved Fe (Figs. 8, 9 and S7), which indicates the suppression of the proton + oxalate-
536 promoted dissolution at $\text{pH} < 2$. In Fig. 10, the model estimates of surface concentration of dissolved Fe over the Bay of Bengal
537 considerably improved in Test 1 compared to Test 0. The model results in Test 1 also indicate a larger contribution of pyrogenic
538 dissolved Fe over regions with strong anthropogenic source such as East Asia, but a smaller contribution downwind from
539 tropical biomass burning regions (Fig. 11). We demonstrated that the implementation of the new Fe dissolution scheme,



540 including a rapid Fe release at the initial stage and highly acidic conditions, enhanced the model estimates. However, in Test
541 1, we turned off the photo-reductive dissolution scheme (Ito, 2015), which was based on the laboratory measurements in Chen
542 and Grassian (2013). To determine the photoinduced dissolution kinetic of CFA particles it is necessary to account for the
543 effect of high concentration of $(\text{NH}_4)_2\text{SO}_4$ on photo-reductive dissolution rate which should be considered in future research.

544 **Data availability statement**

545 The new dissolution schemes for the proton-promoted and oxalate-promoted dissolution are reported in Table 1. Table S1
546 reports the concentrations of H_2SO_4 , $\text{H}_2\text{C}_2\text{O}_4$ and $(\text{NH}_4)_2\text{SO}_4$ in the experiment solutions, the original and final pH from model
547 estimates (including H^+ concentrations and activities), and the pH measurements for the solution with low ionic strength. Table
548 S2 contains the summary of the concentration and activity of total oxalate ions, $\text{C}_2\text{O}_4^{2-}$, and HC_2O_4^- in the experiment solutions
549 calculated using the E-AIM model III. The observations of the surface concentration of aerosol Fe, dissolved Fe and Fe
550 solubility for the fine mode ($\text{PM}_{2.5}$) over the Bay of Bengal are from Bikkina et al. (2020) and are available at
551 <https://pubs.acs.org/doi/10.1021/acsearthspacechem.0c00063>. The Fe speciation, the measurements of the Fe dissolution
552 kinetic, and the results of the IMPACT model for each sensitivity simulation (Test 0-3) can be downloaded at:
553 <https://doi.org/10.25500/edata.bham.00000702>.

554 **Author contributions**

555 CB, ZS, and AI designed the experiments and discussed the results. ZS supervised the experimental and data analyses. CB
556 conducted the experiments and the data analysis with contributions from ZS, AI, MDK and ND. ND, ZS and KI performed
557 the XANES measurements. AI developed the model of the dissolution kinetics and performed the model simulations. Krakow
558 and Aberthaw ash were provided by TJ, while Shandong ash was provided by WL. Soil 5 from Libya was collected by ND.
559 CB prepared the article with contributions from MDK and all the other co-authors.

560 **Competing interests**

561 The authors declare that they have no conflict of interest.

562 **Acknowledgments**

563 CB is funded by the Natural Environment Research Council (NERC) CENTA studentship (grant no. NE/L002493/1). Support
564 for this research was provided to AI by JSPS KAKENHI (grant no. 20H04329), Integrated Research Program for Advancing
565 Climate Models (TOUGOU) (grant no. JPMXD0717935715) from the Ministry of Education, Culture, Sports, Science and
566 Technology (MEXT), Japan. We acknowledge Diamond Light Source for time on Beamline/Lab I18 under the Proposals:
567 SP22244-1; SP12760-1; SP10327-1.

568 **Financial support**

569 This research has been supported by the Natural Environment Research Council (grant no. NE/L002493/1), JSPS KAKENHI
570 (grant no. 20H04329), the Integrated Research Program for Advancing Climate Models (TOUGOU) (grant no.
571 JPMXD0717935715).



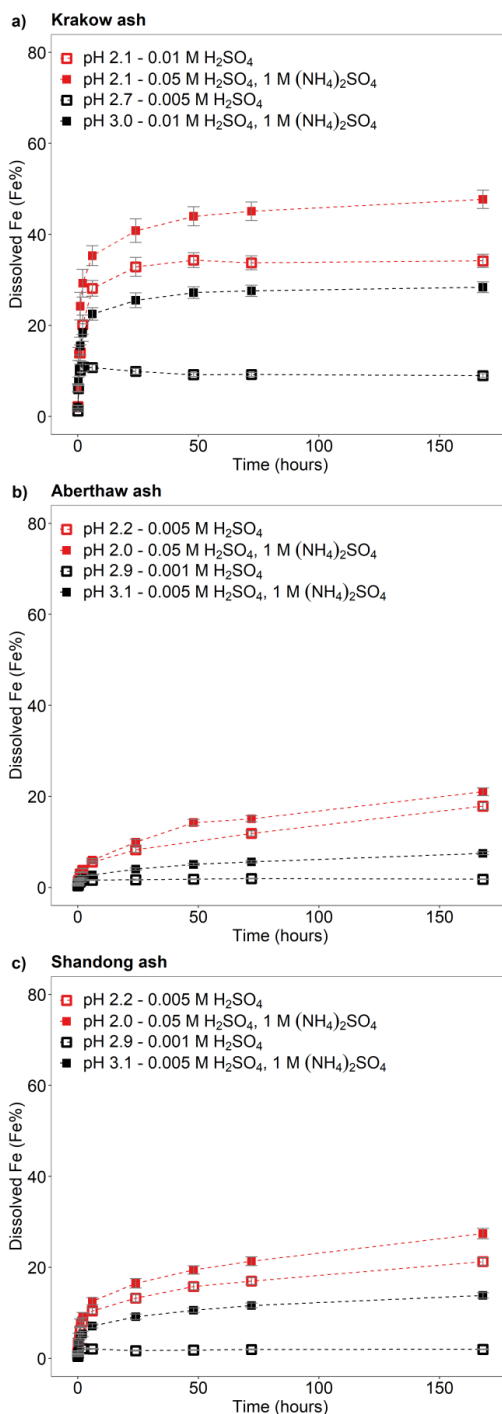
572 **Table 1. Constants used to calculate Fe dissolution rates for fossil fuel combustion aerosols, based on laboratory experiments**
573 **conducted at high ionic strength.**

Stage	Kinetic	Scheme	Rate constant - $k(\text{pH}, T)^a$	m^c
I	Fast	Proton	$7.61 \times 10^{-6} \exp[E(\text{pH})^b \times (1/298 - 1/T)]$	0.241
II	Intermediate	Proton	$1.91 \times 10^{-7} \exp[E(\text{pH})^b \times (1/298 - 1/T)]$	0.195
III	Slow	Proton	$2.48 \times 10^{-7} \exp[E(\text{pH})^b \times (1/298 - 1/T)]$	0.843
I	Fast	Proton + Oxalate	$5.54 \times 10^{-6} \exp[E(\text{pH})^b \times (1/298 - 1/T)]$	0.209
II	Intermediate	Proton + Oxalate	$1.50 \times 10^{-7} \exp[E(\text{pH})^b \times (1/298 - 1/T)]$	0.091
III	Slow	Proton + Oxalate	$1.77 \times 10^{-8} \exp[E(\text{pH})^b \times (1/298 - 1/T)]$	0.204

574 ^a $k(\text{pH}, T)$ is the pH and temperature dependent ‘far-from-equilibrium’ rate constant ($\text{moles Fe g}^{-1} \text{ s}^{-1}$). The Fe dissolution
575 scheme assumes 3 rate constants “fast”, “intermediate” and “slow” for the proton- and oxalate-promoted dissolution. The
576 parameters were fit to our measurements for Krakow ash.

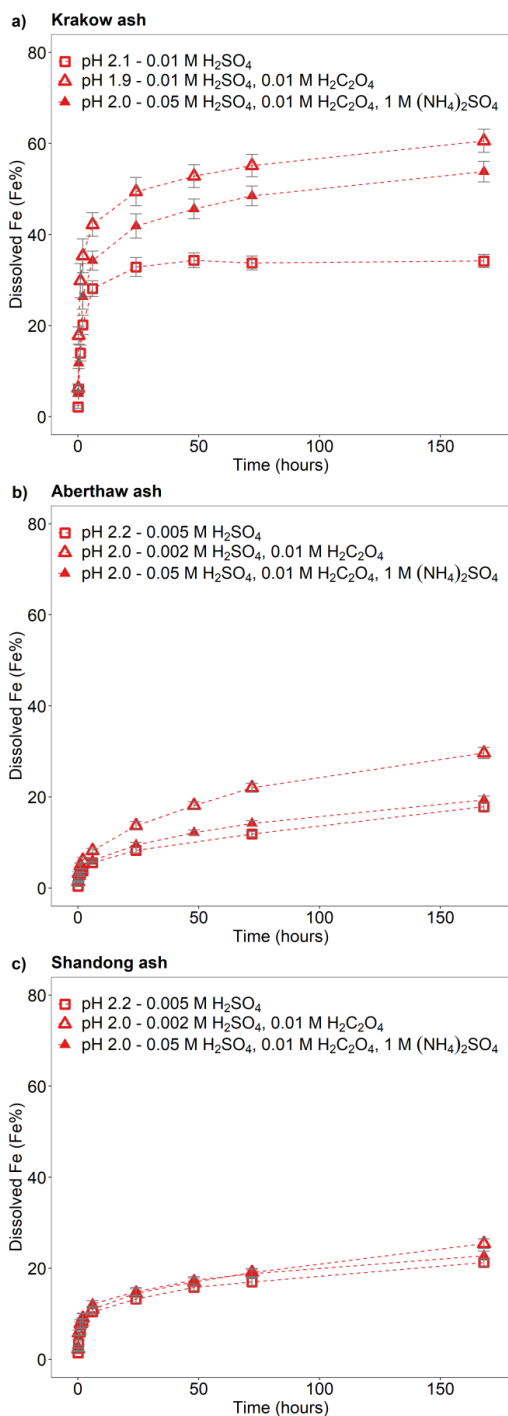
577 ^b $E(\text{pH}) = -1.56 \times 10^3 \times \text{pH} + 1.08 \times 10^4$. The parameters were fit to the measurements for soils (Bibi et al., 2014).

578 ^c m is the reaction order with respect to aqueous phase protons, which was determined by linear regression from our
579 experimental data in the pH range between 2 and 3 for proton- and oxalate-promoted dissolution schemes.
580



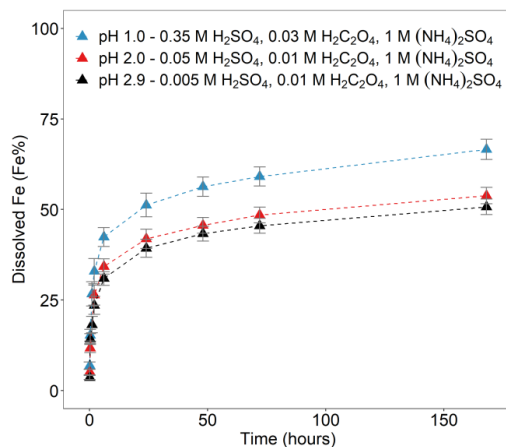
581

582 **Figure 1: Fe dissolution kinetics of a) Krakow ash, b) Aberthaw ash and c) Shandong ash in H₂SO₄ solutions (open rectangles) and**
583 **with 1 M (NH₄)₂SO₄ (filled rectangles). The molar concentrations of H₂SO₄ and (NH₄)₂SO₄ in the experiment solutions are shown.**
584 **The final pH of the experiment solutions is also reported, which was calculated using the E-AIM model III for aqueous solution**
585 **(Wexler and Clegg, 2002) accounting for the buffer capacity of the CFA samples (Experiments 1-2 in Table S1). The experiments**
586 **conducted at around pH 2 are in red, while the experiments at around pH 3 are in black. The data uncertainty was estimated using**
587 **the error propagation formula.**



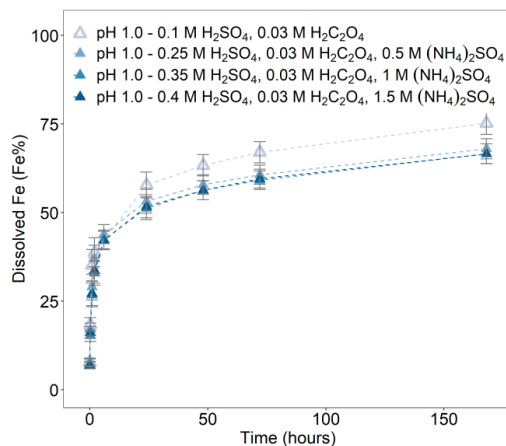
588

589 **Figure 2:** Fe dissolution kinetics of a) Krakow ash, b) Aberthaw ash, and c) Shandong ash in H₂SO₄ solutions at around pH 2 (red
590 open rectangles), with 0.01 M H₂C₂O₄ (red open triangles), and 1 M (NH₄)₂SO₄ (red filled triangles). The molar concentrations of
591 H₂SO₄, H₂C₂O₄ and (NH₄)₂SO₄ in the experiment solutions are shown. The final pH of the experiment solutions is also reported,
592 which was calculated using the E-AIM model III for aqueous solution (Wexler and Clegg, 2002) accounting for the buffer capacity
593 of the CFA samples (Experiments 1, 3-4 at around pH 2). The data uncertainty was estimated using the error propagation formula.



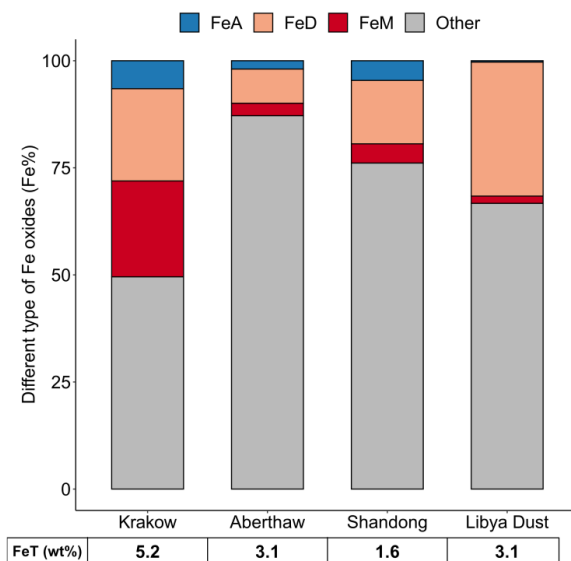
594

595 **Figure 3:** Fe dissolution kinetics of Krakow ash in H_2SO_4 solutions at pH 1.0 with 0.03 M $\text{H}_2\text{C}_2\text{O}_4$ and 1 M $(\text{NH}_4)_2\text{SO}_4$ (blue filled
596 triangles), at pH 2.0 with 0.01 M $\text{H}_2\text{C}_2\text{O}_4$ and 1 M $(\text{NH}_4)_2\text{SO}_4$ (red filled triangles), and at pH 2.9 with 0.01 M $\text{H}_2\text{C}_2\text{O}_4$ and 1 M
597 $(\text{NH}_4)_2\text{SO}_4$ (black filled triangles). The molar concentrations of H_2SO_4 , $\text{H}_2\text{C}_2\text{O}_4$ and $(\text{NH}_4)_2\text{SO}_4$ in the experiment solutions are shown.
598 The final pH of the experiment solutions is also reported, which was calculated using the E-AIM model III for aqueous solution
599 (Wexler and Clegg, 2002) accounting for the buffer capacity of the CFA samples (Experiment 7 at pH 1.0, Experiment 3 at pH 2.0,
600 and Experiment 3 at pH 2.9 in Table S1). The data uncertainty was estimated using the error propagation formula.



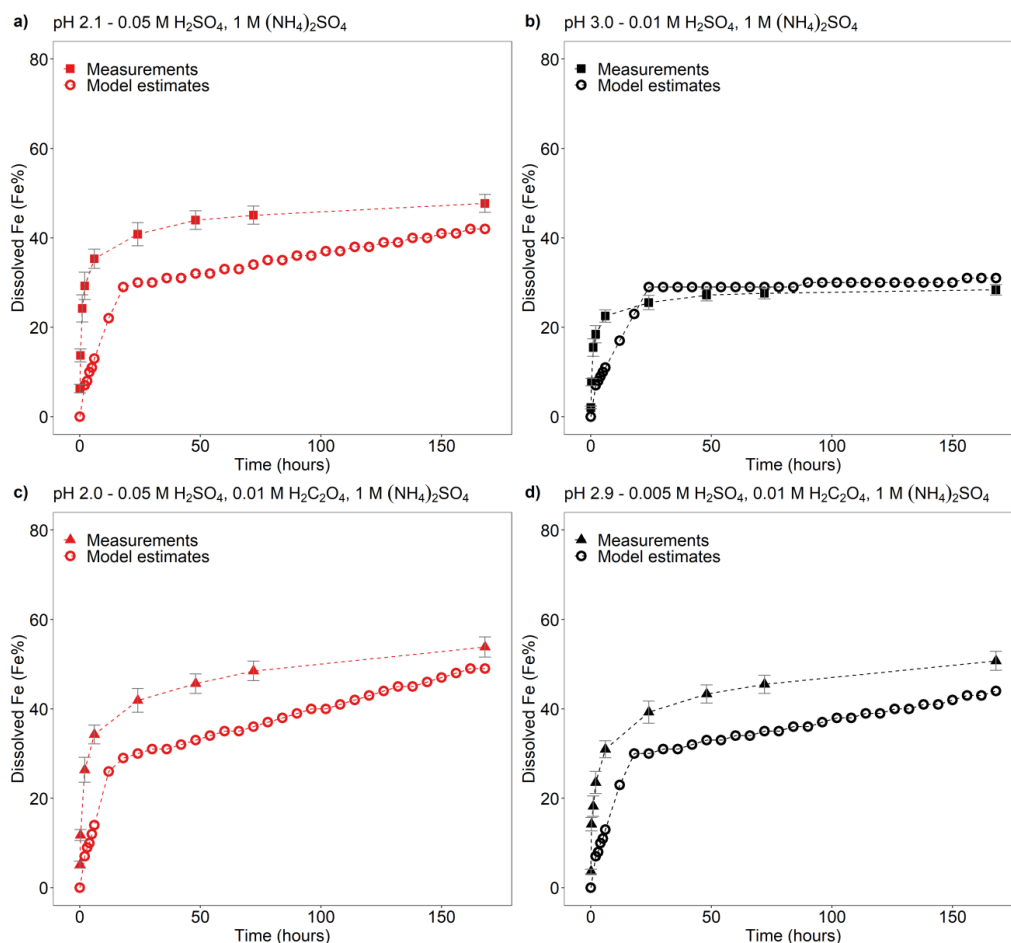
601

602 **Figure 4:** Fe dissolution kinetics of Krakow ash in H_2SO_4 solutions at pH 1.0 with 0.03 M $\text{H}_2\text{C}_2\text{O}_4$ and concentration of $(\text{NH}_4)_2\text{SO}_4$
603 from 0 to 1.5 M. The molar concentrations of H_2SO_4 , $\text{H}_2\text{C}_2\text{O}_4$ and $(\text{NH}_4)_2\text{SO}_4$ in the experiment solutions are shown. The final pH of
604 the experiment solutions is also reported, which was calculated using the E-AIM model III for aqueous solution (Wexler and Clegg,
605 2002) accounting for the buffer capacity of the CFA samples (Experiments 5-8 in Table S1). The data uncertainty was estimated
606 using the error propagation formula.



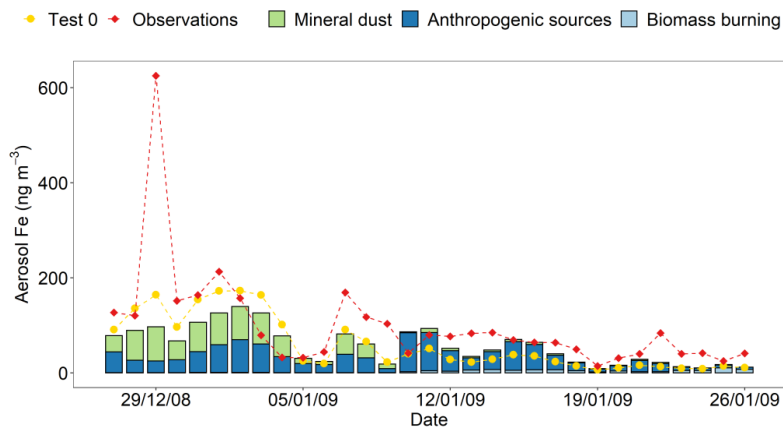
607

608 **Figure 5: Percentages of ascorbate Fe (FeA), dithionite Fe (FeD), magnetite Fe (FeM) and other Fe to the total Fe (FeT) in the coal**
 609 **fly ash samples and mineral dust from Africa (Libya dust). The FeT (as %wt.) was given below each sample column. The data**
 610 **uncertainty was estimated using the error propagation formula: 4% for FeA/FeT, 11% for FeD/FeT, 12% for FeM/FeT, and 2 %**
 611 **for FeT.**



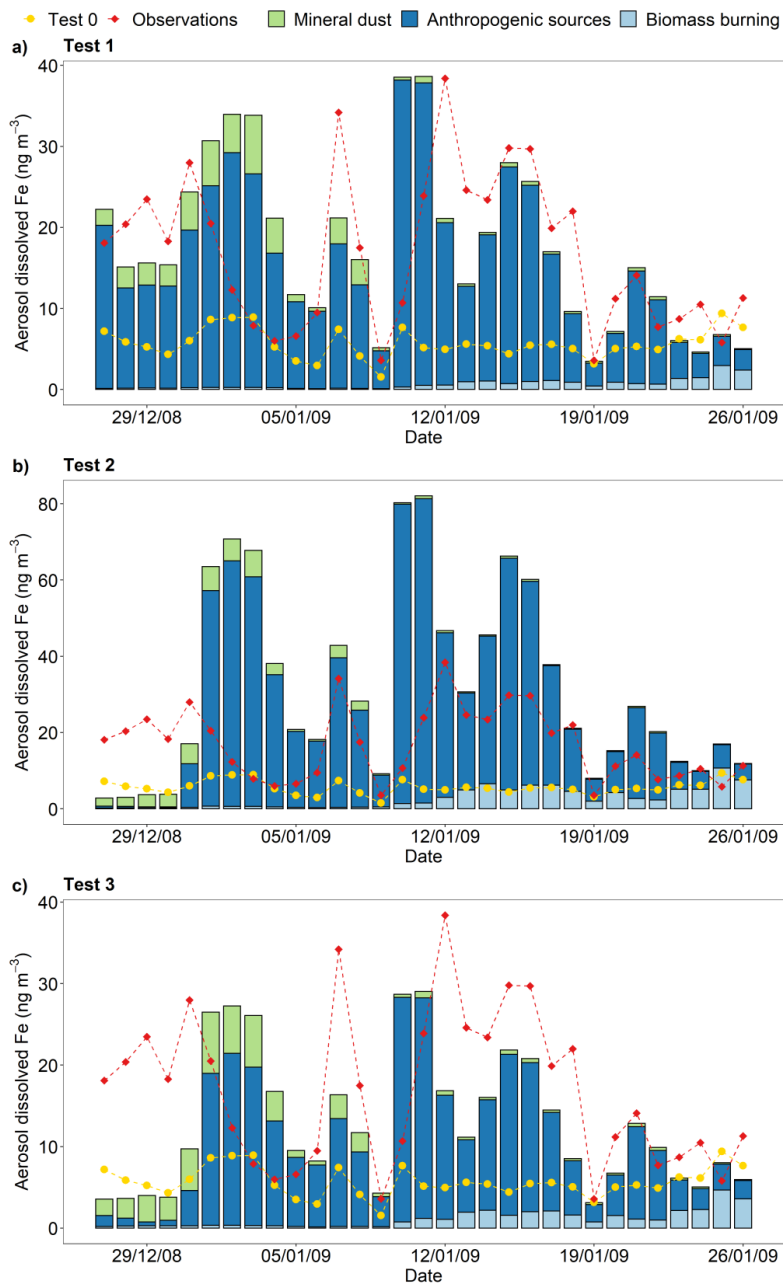
612

613 **Figure 6: Comparison between the Fe dissolution kinetics of Krakow ash predicted using Eq. (1) and measured in H₂SO₄ solutions**
614 **a-b) with 1 M (NH₄)₂SO₄, c-d) with 0.01 M H₂C₂O₄ and 1 M (NH₄)₂SO₄. The molar concentrations of H₂SO₄, H₂C₂O₄ and (NH₄)₂SO₄**
615 **in the experiment solutions are shown. The final pH of the experiment solutions is also reported, which was calculated using the E-**
616 **AIM model III for aqueous solution (Wexler and Clegg, 2002) accounting for the buffer capacity of the CFA samples (Experiments**
617 **2-3 in Table S1). The experiments conducted at around pH 2 are in red, while the experiments at around pH 3 are in black. The data**
618 **uncertainty was estimated using the error propagation formula.**



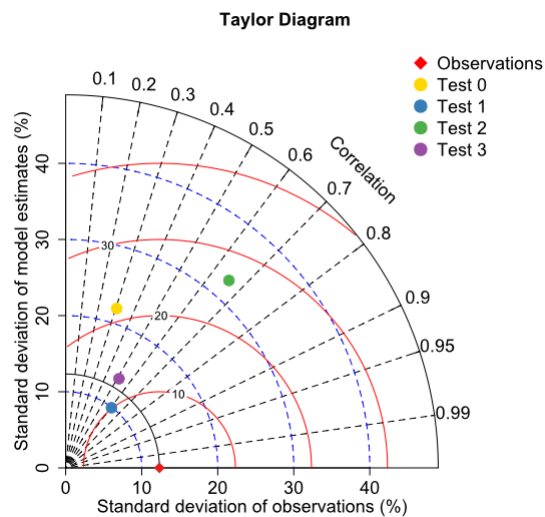
619

620 **Figure 7: Surface concentration of Fe in PM_{2.5} aerosol particles over the Bay of Bengal from 27 December 2008 to 26 January 2009.**
621 **Observations are from Bikkina et al. (2020) (red filled diamonds). Aerosol Fe was calculated along the cruise tracks using the**
622 **IMPACT model. The total Fe emission in anthropogenic aerosols was estimated using Fe emission factors by each sector such as**
623 **energy, industry, and iron and steel industry for the simulation years (Ito et al., 2018) in sensitivity Test 0 (yellow filled circles), while**
624 **the mineral specific emission inventory for the year 2010 by Rathod et al. (2020) was used in the other tests. The contribution of**
625 **mineral dust sources, anthropogenic sources and biomass burning to total Fe is shown for Test 1-3.**



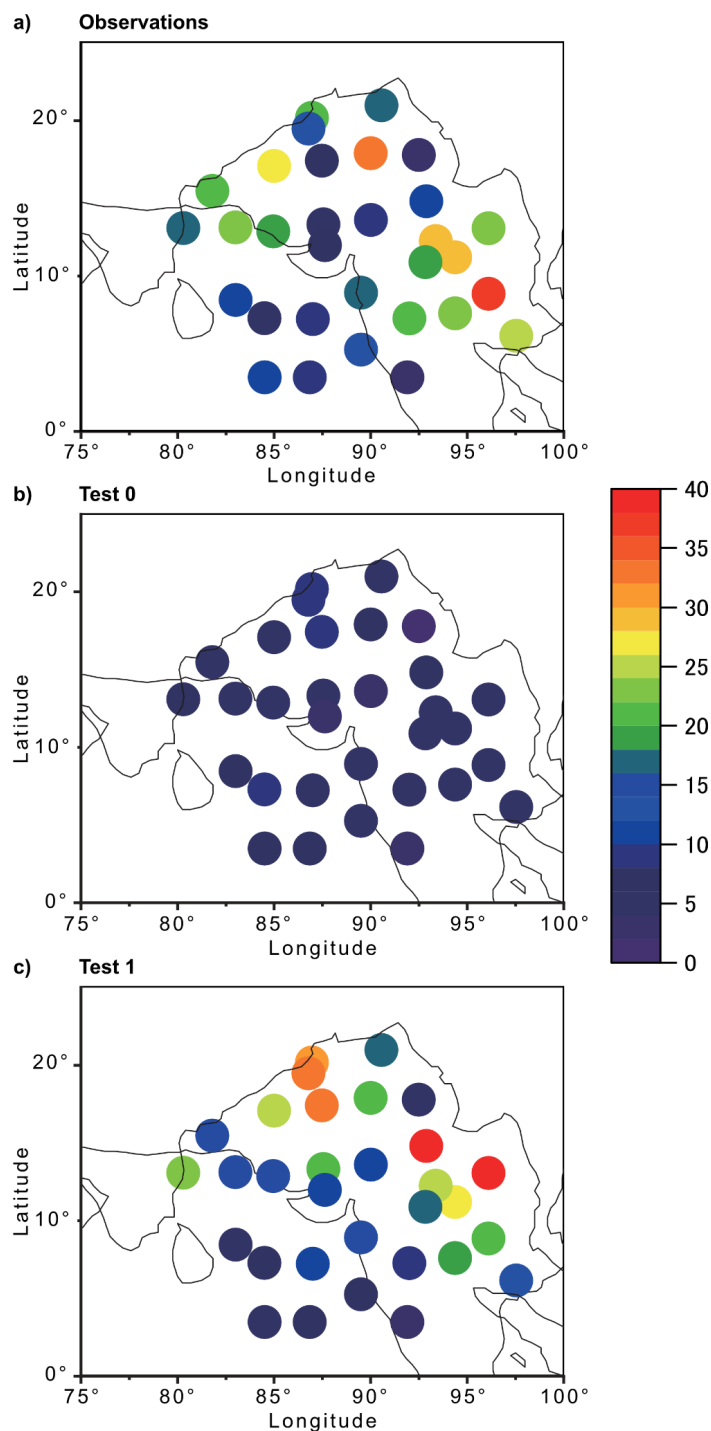
626

627 **Figure 8:** Surface concentration of dissolved Fe in PM_{2.5} aerosol particles over the Bay of Bengal from 27 December 2008 to 26
628 January 2009. Observations are from Bikkina et al. (2020) (red filled diamonds). Aerosol dissolved Fe was calculated along the cruise
629 tracks using the IMPACT model. In Test 0 (yellow filled circles), we ran the model without upgrades in the Fe dissolution scheme
630 (Ito et al., 2021a), and applying the proton-promoted, oxalate-promoted and photoinduced dissolution schemes for combustion
631 aerosols. The contribution of mineral dust sources, anthropogenic sources and biomass burning is shown for Test 1-3. The proton +
632 oxalate dissolution scheme (Table 1) was applied in Test 1 and 3, while proton-promoted dissolution is used for Test 2. We adopted
633 the mineral-specific inventory for anthropogenic Fe emissions (Rathod et al., 2020) in Test 1 and 2. In Test 3, the Fe speciation of
634 Krakow ash was used for all combustion sources.



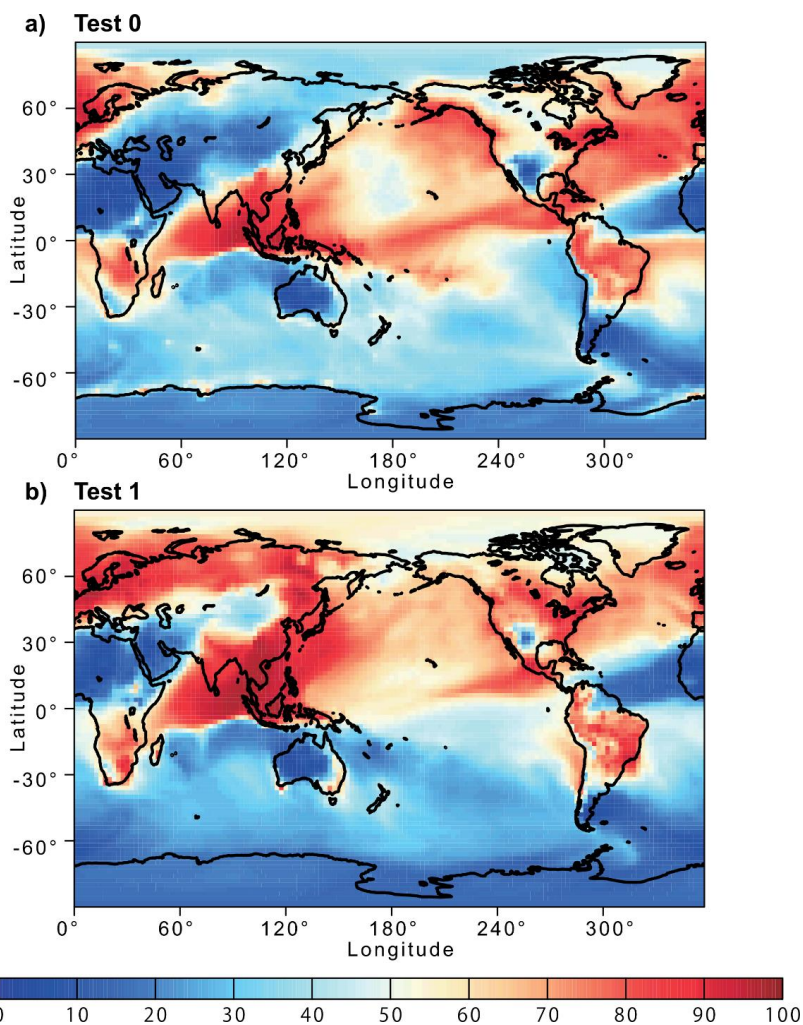
635

636 **Figure 9: Comparison between observations and model estimates of Fe solubility in $PM_{2.5}$ aerosol particles over the Bay of Bengal**
637 **from 27 December 2008 to 26 January 2009. Observations are from Bikkina et al. (2020). Aerosol Fe solubility was calculated along**
638 **the cruise tracks using the IMPACT model. The Taylor diagram summarizes the statistics for the comparison between observations**
639 **of aerosol Fe solubility and the different simulations (Test 0-3). The dashed curves in blue indicate the standard deviation values.**
640 **The curves in red denote the root-mean-squared difference between the observational data and the model predictions. The dashed**
641 **lines in black represent the correlation coefficients.**



642

643 **Figure 10:** Surface concentration of dissolved Fe in PM_{2.5} aerosol particles over the Bay of Bengal from 27 December 2008 to 26
644 January 2009. a) Observations from Bikkina et al. (2020). b-c) Aerosol dissolved Fe calculated along the cruise tracks using the
645 IMPACT model. In Test 0, we ran the model without upgrades in the Fe dissolution scheme (Ito et al., 2021a) and applying the
646 proton-promoted, oxalate-promoted and photoinduced dissolution schemes for combustion aerosols Table S3 (Ito, 2015). The proton
647 + oxalate dissolution scheme (Table 1) was applied in Test 1 and we adopted the mineral-specific inventory for anthropogenic Fe
648 emissions (Rathod et al., 2020).



649

650 **Figure 11: Proportion (%) of pyrogenic dissolved Fe in aerosol dissolved Fe concentration near the surface from a) Test 0 and b)**
651 **Test 1 for December 2008 and January 2009. In Test 0, we ran the model without upgrades in the Fe dissolution scheme (Ito et al.,**
652 **2021a) and applying the proton-promoted, oxalate-promoted and photoinduced dissolution schemes for combustion aerosols Table**
653 **S3 (Ito, 2015). The proton + oxalate dissolution scheme (Table 1) was applied in Test 1 and we adopted the mineral-specific inventory**
654 **for anthropogenic Fe emissions (Rathod et al., 2020).**

655



656 **References**

- 657 Baker, A. R., Li, M., and Chance, R.: Trace Metal Fractional Solubility in Size-Segregated Aerosols From the Tropical Eastern
658 Atlantic Ocean, *Global Biogeochem.*, 34, e2019GB006510, doi: 10.1029/2019GB006510, 2020.
- 659 Baker, A. R., Kanakidou, M., Nenes, A., Myriokefalitakis, S., Croot, P. L., Duce, R. A., Gao, Y., Guieu, C., Ito, A., Jickells,
660 T. D., Mahowald, N. M., Middag, R., Perron, M. M. G., Sarin, M. M., Shelley, R., and Turner, D. R.: Changing atmospheric
661 acidity as a modulator of nutrient deposition and ocean biogeochemistry, *Sci. Adv.*, 7, eabd8800, doi: 10.1126/sciadv.abd8800,
662 2021.
- 663 Baldo, C., Formenti, P., Nowak, S., Chevaillier, S., Cazaunau, M., Pangu, E., Di Biagio, C., Doussin, J. F., Ignatyev, K.,
664 Dagsson-Waldhauserova, P., Arnalds, O., MacKenzie, A. R., and Shi, Z.: Distinct chemical and mineralogical composition of
665 Icelandic dust compared to northern African and Asian dust, *Atmos. Chem. Phys.*, 20, 13521-13539, doi: 10.5194/acp-20-
666 13521-2020, 2020.
- 667 Bibi, I., Singh, B., and Silvester, E.: Dissolution kinetics of soil clays in sulfuric acid solutions: Ionic strength and temperature
668 effects, *Appl. Geochem.*, 51, 170-183, doi: 10.1016/j.apgeochem.2014.10.004, 2014.
- 669 Bikkina, S., Kawamura, K., Sarin, M., and Tachibana, E.: ¹³C Probing of Ambient Photo-Fenton Reactions Involving Iron and
670 Oxalic Acid: Implications for Oceanic Biogeochemistry, *ACS Earth Space Chem.*, 4, 964-976, doi:
671 10.1021/acsearthspacechem.0c00063, 2020.
- 672 Blissett, R. S., and Rowson, N. A.: A review of the multi-component utilisation of coal fly ash, *Fuel*, 97, 1-23, doi:
673 10.1016/j.fuel.2012.03.024, 2012.
- 674 Borgatta, J., Paskavitz, A., Kim, D., and Navea, J. G.: Comparative evaluation of iron leach from different sources of fly ash
675 under atmospherically relevant conditions, *Environ. Chem.*, 13, 902-912, doi: 10.1071/en16046, 2016.
- 676 Boyd, P. W., Jickells, T., Law, C. S., Blain, S., Boyle, E. A., Buesseler, K. O., Coale, K. H., Cullen, J. J., de Baar, H. J. W.,
677 Follows, M., Harvey, M., Lancelot, C., Levasseur, M., Owens, N. P. J., Pollard, R., Rivkin, R. B., Sarmiento, J., Schoemann,
678 V., Smetacek, V., Takeda, S., Tsuda, A., Turner, S., and Watson, A. J.: Mesoscale Iron Enrichment Experiments 1993-2005:
679 Synthesis and Future Directions, *Science*, 315, 612-617, doi: 10.1126/science.1131669, 2007.
- 680 British Petroleum (BP): Statistical Review of World Energy 2020, available at
681 <https://www.bp.com/en/global/corporate/energy-economics/statistical-review-of-world-energy.html>, (last access: 10 April
682 2021), 2020.
- 683 Brown, P., Jones, T., and Bérubé, K.: The internal microstructure and fibrous mineralogy of fly ash from coal-burning power
684 stations, *Environ. Pollut.*, 159, 3324-3333, doi: 10.1016/j.envpol.2011.08.041, 2011.
- 685 Chen, H., Laskin, A., Baltrusaitis, J., Gorski, C. A., Scherer, M. M., and Grassian, V. H.: Coal fly ash as a source of iron in
686 atmospheric dust, *Environ. Sci. Technol.*, 46, 2112-2120, doi: 10.1021/es204102f, 2012.
- 687 Chen, H. H., and Grassian, V. H.: Iron Dissolution of Dust Source Materials during Simulated Acidic Processing: The Effect
688 of Sulfuric, Acetic, and Oxalic Acids, *Environ. Sci. Technol.*, 47, 10312-10321, doi: 10.1021/es401285s, 2013.
- 689 Cornell, R. M., Posner, A. M., and Quirk, J. P.: Kinetics and mechanisms of the acid dissolution of goethite (α -FeOOH),
690 *Journal of Inorganic and Nuclear Chemistry*, 38, 563-567, doi: 10.1016/0022-1902(76)80305-3, 1976.
- 691 Cornell, R. M., and Schwertmann, U.: *The Iron Oxides: Structure, Properties, Reactions, Occurrence and Uses*, Wiley-VCH,
692 New York 2003.
- 693 Cwiertny, D. M., Baltrusaitis, J., Hunter, G. J., Laskin, A., Scherer, M. M., and Grassian, V. H.: Characterization and acid-
694 mobilization study of iron-containing mineral dust source materials, *J. Geophys. Res.-Atmos.*, 113, D05202, doi:
695 10.1029/2007jd009332, 2008.
- 696 Dudas, M. J., and Warren, C. J.: Submicroscopic model of fly ash particles, *Geoderma*, 40, 101-114, doi: 10.1016/0016-
697 7061(87)90016-4, 1987.
- 698 Eick, M. J., Peak, J. D., and Brady, W. D.: The Effect of Oxyanions on the Oxalate-Promoted Dissolution of Goethite, *SSSAJ*,
699 63, 1133-1141, doi: doi.org/10.2136/sssaj1999.6351133x, 1999.



- 700 Emerson, E. W., Hodshire, A. L., DeBolt, H. M., Bilsback, K. R., Pierce, J. R., McMeeking, G. R., and Farmer, D. K.:
701 Revisiting particle dry deposition and its role in radiative effect estimates, *PNAS USA*, 117, 26076-26082, doi:
702 10.1073/pnas.2014761117, 2020.
- 703 Fu, H., Cwiertny, D. M., Carmichael, G. R., Scherer, M. M., and Grassian, V. H.: Photoreductive dissolution of Fe-containing
704 mineral dust particles in acidic media, *Journal of Geophysical Research*, 115, D11304, doi: 10.1029/2009jd012702, 2010.
- 705 Fu, H. B., Lin, J., Shang, G. F., Dong, W. B., Grassian, V. H., Carmichael, G. R., Li, Y., and Chen, J. M.: Solubility of Iron
706 from Combustion Source Particles in Acidic Media Linked to Iron Speciation, *Environ. Sci. Technol.*, 46, 11119-11127, doi:
707 10.1021/es302558m, 2012.
- 708 Furrer, G., and Stumm, W.: The coordination chemistry of weathering: I. Dissolution kinetics of δ -Al₂O₃ and BeO, *Geochim.*
709 *Cosmochim. Ac.*, 50, 1847-1860, doi: 10.1016/0016-7037(86)90243-7, 1986.
- 710 Hamer, M., Graham, R. C., Amrhein, C., and Bozhilov, K. N.: Dissolution of ripidolite (Mg, Fe-chlorite) in organic and
711 inorganic acid solutions, *SSSAJ*, 67, 654-661, doi: 10.2136/sssaj2003.6540, 2003.
- 712 Ito, A., and Feng, Y.: Role of dust alkalinity in acid mobilization of iron, *Atmos. Chem. Phys.*, 10, 9237-9250, doi:
713 10.5194/acp-10-9237-2010, 2010.
- 714 Ito, A.: Atmospheric Processing of Combustion Aerosols as a Source of Bioavailable Iron, *Environ. Sci. Technol. Lett.*, 2, 70-
715 75, doi: 10.1021/acs.estlett.5b00007, 2015.
- 716 Ito, A., and Shi, Z.: Delivery of anthropogenic bioavailable iron from mineral dust and combustion aerosols to the ocean,
717 *Atmos. Chem. Phys.*, 16, 85-99, doi: 10.5194/acp-16-85-2016, 2016.
- 718 Ito, A., Lin, G. X., and Penner, J. E.: Radiative forcing by light-absorbing aerosols of pyrogenic iron oxides, *Sci. Rep.*, 8,
719 7347, doi: 10.1038/s41598-018-25756-3, 2018.
- 720 Ito, A., Myriokefalitakis, S., Kanakidou, M., Mahowald, N. M., Scanza, R. A., Hamilton, D. S., Baker, A. R., Jickells, T.,
721 Sarin, M., Bikkina, S., Gao, Y., Shelley, R. U., Buck, C. S., Landing, W. M., Bowie, A. R., Perron, M. M. G., Guieu, C.,
722 Meskhidze, N., Johnson, M. S., Feng, Y., Kok, J. F., Nenes, A., and Duce, R. A.: Pyrogenic iron: The missing link to high iron
723 solubility in aerosols, *Sci. Adv.*, 5, eaau7671 doi: 10.1126/sciadv.aau7671, 2019.
- 724 Ito, A., Adebisi, A. A., Huang, Y., and Kok, J. F.: Less atmospheric radiative heating due to aspherical dust with coarser size,
725 *Atmos. Chem. Phys. Discuss.*, 2021, 1-44, doi: 10.5194/acp-2021-134, 2021a.
- 726 Ito, A., Ye, Y., Baldo, C., and Shi, Z.: Ocean fertilization by pyrogenic aerosol iron, *npj Clim. Atmos. Sci.*, 4, 30, doi:
727 10.1038/s41612-021-00185-8, 2021b.
- 728 Jickells, T., and Moore, C. M.: The importance of Atmospheric Deposition for Ocean Productivity, *Annu. Rev. Ecol. Evol.*
729 *Syst.*, 46, 481-501, doi: 10.1146/annurev-ecolsys-112414-054118, 2015.
- 730 Jickells, T. D., An, Z. S., Andersen, K. K., Baker, A. R., Bergametti, G., Brooks, N., Cao, J. J., Boyd, P. W., Duce, R. A.,
731 Hunter, K. A., Kawahata, H., Kubilay, N., laRoche, J., Liss, P. S., Mahowald, N., Prospero, J. M., Ridgwell, A. J., Tegen, I.,
732 and Torres, R.: Global iron connections between desert dust, ocean biogeochemistry, and climate, *Science*, 308, 67-71, doi:
733 10.1126/science.1105959, 2005.
- 734 Jones, D. R.: The Leaching of Major and Trace Elements from Coal Ash, in: *Environmental Aspects of Trace Elements in*
735 *Coal*, edited by: Swaine, D. J., and Goodarzi, F., Springer Netherlands, Dordrecht, 221-262, 1995.
- 736 Kanakidou, M., Myriokefalitakis, S., and Tsigaridis, K.: Aerosols in atmospheric chemistry and biogeochemical cycles of
737 nutrients, *Environ. Res. Lett.*, 13, 063004, doi: 10.1088/1748-9326/aabcb, 2018.
- 738 Kawamura, K., and Bikkina, S.: A review of dicarboxylic acids and related compounds in atmospheric aerosols: Molecular
739 distributions, sources and transformation, *Atmos. Res.*, 170, 140-160, doi: 10.1016/j.atmosres.2015.11.018, 2016.
- 740 Kim, D., Xiao, Y., Karchere-Sun, R., Richmond, E., Ricker, H. M., Leonardi, A., and Navea, J. G.: Atmospheric Processing
741 of Anthropogenic Combustion Particles: Effects of Acid Media and Solar Flux on the Iron Mobility from Fly Ash, *ACS Earth*
742 *Space Chem.*, 4, 750-761, doi: 10.1021/acsearthspacechem.0c00057, 2020.
- 743 Kukier, U., Ishak, C. F., Sumner, M. E., and Miller, W. P.: Composition and element solubility of magnetic and non-magnetic
744 fly ash fractions, *Environ. Pollut.*, 123, 255-266, doi: 10.1016/S0269-7491(02)00376-7, 2003.



- 745 Kumar, A., Sarin, M. M., and Srinivas, B.: Aerosol iron solubility over Bay of Bengal: Role of anthropogenic sources and
746 chemical processing, *Mar. Chem.*, 121, 167-175, doi: 10.1016/j.marchem.2010.04.005, 2010.
- 747 Kutchko, B. G., and Kim, A. G.: Fly ash characterization by SEM–EDS, *Fuel*, 85, 2537-2544, doi: 10.1016/j.fuel.2006.05.016,
748 2006.
- 749 Lawson, M. J., Prytherch, Z. C., Jones, T. P., Adams, R. A., and Bérubé, K. A.: Iron-Rich Magnetic Coal Fly Ash Particles
750 Induce Apoptosis in Human Bronchial Cells, *Appl. Sci.*, 10, 8368, doi: 10.3390/app10238368, 2020.
- 751 Lee, S. O., Tran, T., Jung, B. H., Kim, S. J., and Kim, M. J.: Dissolution of iron oxide using oxalic acid, *Hydrometallurgy*, 87,
752 91-99, doi: 10.1016/j.hydromet.2007.02.005, 2007.
- 753 Li, J., Anderson, J. R., and Buseck, P. R.: TEM study of aerosol particles from clean and polluted marine boundary layers over
754 the North Atlantic, *J. Geophys. Res.-Atmos.*, 108, doi: 10.1029/2002JD002106, 2003.
- 755 Li, W. J., Xu, L., Liu, X. H., Zhang, J. C., Lin, Y. T., Yao, X. H., Gao, H. W., Zhang, D. Z., Chen, J. M., Wang, W. X.,
756 Harrison, R. M., Zhang, X. Y., Shao, L. Y., Fu, P. Q., Nenes, A., and Shi, Z. B.: Air pollution-aerosol interactions produce
757 more bioavailable iron for ocean ecosystems, *Sci. Adv.*, 3, e1601749, doi: 10.1126/sciadv.1601749, 2017.
- 758 Mahowald, N. M., Kloster, S., Engelstaedter, S., Moore, J. K., Mukhopadhyay, S., McConnell, J. R., Albani, S., Doney, S. C.,
759 Bhattacharya, A., Curran, M. A. J., Flanner, M. G., Hoffman, F. M., Lawrence, D. M., Lindsay, K., Mayewski, P. A., Neff, J.,
760 Rothenberg, D., Thomas, E., Thornton, P. E., and Zender, C. S.: Observed 20th century desert dust variability: impact on
761 climate and biogeochemistry, *Atmos. Chem. Phys.*, 10, 10875-10893, doi: 10.5194/acp-10-10875-2010, 2010.
- 762 Marcotte, A. R., Anbar, A. D., Majestic, B. J., and Herckes, P.: Mineral Dust and Iron Solubility: Effects of Composition,
763 Particle Size, and Surface Area, *Atmosphere*, 11, 533, doi: 10.3390/atmos11050533, 2020.
- 764 Martin, J. H.: Glacial-interglacial CO₂ change: The Iron Hypothesis, *Paleoceanography*, 5, 1-13, doi:
765 10.1029/PA005i001p00001, 1990.
- 766 Matsuo, M., Kobayashi, T., Singh, T. B., Tsurumi, M., and Ichikuni, M.: ⁵⁷Fe Mössbauer spectroscopic study of Japanese
767 cedar bark — The variation in chemical states of iron due to influence of human activities, *Hyperfine Interact.*, 71, 1255-1258,
768 doi: 10.1007/BF02397311, 1992.
- 769 Meskhidze, N., Chameides, W. L., Nenes, A., and Chen, G.: Iron mobilization in mineral dust: Can anthropogenic SO₂
770 emissions affect ocean productivity?, *Geophys. Res. Lett.*, 30, 2085, doi: 10.1029/2003gl018035, 2003.
- 771 Mills, M. M., Ridame, C., Davey, M., La Roche, J., and Geider, R. J.: Iron and phosphorus co-limit nitrogen fixation in the
772 eastern tropical North Atlantic, *Nature*, 429, 292-294, doi: 10.1038/nature02550, 2004.
- 773 Moore, C. M., Mills, M. M., Milne, A., Langlois, R., Achterberg, E. P., Lochte, K., Geider, R. J., and La Roche, J.: Iron limits
774 primary productivity during spring bloom development in the central North Atlantic, *Glob. Change Biol.*, 12, 626-634, doi:
775 10.1111/j.1365-2486.2006.01122.x, 2006.
- 776 Munawar, M. E.: Human health and environmental impacts of coal combustion and post-combustion wastes, *J. Sustain. Min.*,
777 17, 87-96, doi: 10.1016/j.jsm.2017.12.007, 2018.
- 778 Myriokefalitakis, S., Ito, A., Kanakidou, M., Nenes, A., Krol, M. C., Mahowald, N. M., Scanza, R. A., Hamilton, D. S.,
779 Johnson, M. S., Meskhidze, N., Kok, J. F., Guieu, C., Baker, A. R., Jickells, T. D., Sarin, M. M., Bikina, S., Shelley, R.,
780 Bowie, A., Perron, M. M. G., and Duce, R. A.: Reviews and syntheses: the GESAMP atmospheric iron deposition model
781 intercomparison study, *Biogeosciences*, 15, 6659-6684, doi: 10.5194/bg-15-6659-2018, 2018.
- 782 Paris, R., Desboeufs, K. V., and Journet, E.: Variability of dust iron solubility in atmospheric waters: Investigation of the role
783 of oxalate organic complexation, *Atmos. Environ.*, 45, 6510-6517, doi: 10.1016/j.atmosenv.2011.08.068, 2011.
- 784 Paris, R., and Desboeufs, K. V.: Effect of atmospheric organic complexation on iron-bearing dust solubility, *Atmos. Chem.*
785 *Phys.*, 13, 4895-4905, doi: 10.5194/acp-13-4895-2013, 2013.
- 786 Poulton, S. W., and Canfield, D. E.: Development of a sequential extraction procedure for iron: implications for iron
787 partitioning in continentally derived particulates, *Chem. Geol.*, 214, 209-221, doi: 10.1016/j.chemgeo.2004.09.003, 2005.
- 788 Pye, H. O. T., Nenes, A., Alexander, B., Ault, A. P., Barth, M. C., Clegg, S. L., Collett Jr, J. L., Fahey, K. M., Hennigan, C.
789 J., Herrmann, H., Kanakidou, M., Kelly, J. T., Ku, I. T., McNeill, V. F., Riemer, N., Schaefer, T., Shi, G., Tilgner, A., Walker,



- 790 J. T., Wang, T., Weber, R., Xing, J., Zaveri, R. A., and Zuend, A.: The acidity of atmospheric particles and clouds, *Atmos. Chem. Phys.*, 20, 4809-4888, doi: 10.5194/acp-20-4809-2020, 2020.
- 792 Raiswell, R., Benning, L. G., Tranter, M., and Tulaczyk, S.: Bioavailable iron in the Southern Ocean: the significance of the iceberg conveyor belt, *Geochemical Transactions*, 9, doi: 10.1186/1467-4866-9-7, 2008.
- 794 Rathod, S. D., Hamilton, D. S., Mahowald, N. M., Klimont, Z., Corbett, J. J., and Bond, T. C.: A Mineralogy - Based Anthropogenic Combustion - Iron Emission Inventory, *J. Geophys. Res.-Atmos.*, 125, e2019JD032114, doi: 10.1029/2019jd032114, 2020.
- 797 Ravel, B., and Newville, M.: ATHENA, ARTEMIS, HEPHAESTUS: data analysis for X-ray absorption spectroscopy using IFEFFIT, *J. Synchrotron Radiat.*, 12, 537-541, doi: 10.1107/S09090495012719, 2005.
- 799 Rubasinghege, G., Lentz, R. W., Scherer, M. M., and Grassian, V. H.: Simulated atmospheric processing of iron oxyhydroxide minerals at low pH: roles of particle size and acid anion in iron dissolution, *PNAS USA*, 107, 6628-6633, doi: 10.1073/pnas.0910809107, 2010.
- 802 Rubin, M., Berman-Frank, I., and Shaked, Y.: Dust- and mineral-iron utilization by the marine dinitrogen-fixer *Trichodesmium*, *Nat. Geosci.*, 4, 529-534, doi: 10.1038/ngeo1181, 2011.
- 804 Schlosser, C., Schmidt, K., Aquilina, A., Homoky, W. B., Castrillejo, M., Mills, R. A., Patey, M. D., Fielding, S., Atkinson, A., and Achterberg, E. P.: Mechanisms of dissolved and labile particulate iron supply to shelf waters and phytoplankton blooms off South Georgia, Southern Ocean, *Biogeosciences*, 15, 4973-4993, doi: 10.5194/bg-15-4973-2018, 2018.
- 807 Schroth, A. W., Crusius, J., Sholkovitz, E. R., and Bostick, B. C.: Iron solubility driven by speciation in dust sources to the ocean, *Nat. Geosci.*, 2, 337-340, doi: 10.1038/ngeo501, 2009.
- 809 Schwertmann, U.: Solubility and dissolution of iron oxides, *Plant Soil*, 130, 1-25, doi: 10.1007/BF00011851, 1991.
- 810 Seinfeld, J. H., and Pandis, S. N.: *Atmospheric chemistry and physics: from air pollution to climate change*, John Wiley & Sons, 2016.
- 812 Shi, Z., Krom, M. D., Bonneville, S., Baker, A. R., Jickells, T. D., and Benning, L. G.: Formation of iron nanoparticles and increase in iron reactivity in the mineral dust during simulated cloud processing, *Environ. Sci. Technol.*, 43, 6592-6596, doi: 10.1021/es901294g, 2009.
- 815 Shi, Z., Bonneville, S., Krom, M. D., Carslaw, K. S., Jickells, T. D., Baker, A. R., and Benning, L. G.: Iron dissolution kinetics of mineral dust at low pH during simulated atmospheric processing, *Atmos. Chem. Phys.*, 11, 995-1007, doi: 10.5194/acp-11-995-2011, 2011a.
- 818 Shi, Z., Krom, M. D., Bonneville, S., Baker, A. R., Bristow, C., Drake, N., Mann, G., Carslaw, K., McQuaid, J. B., Jickells, T., and Benning, L. G.: Influence of chemical weathering and aging of iron oxides on the potential iron solubility of Saharan dust during simulated atmospheric processing, *Global Biogeochem.*, 25, GB2010, doi: 10.1029/2010gb003837, 2011b.
- 821 Shi, Z., Krom, M. D., Jickells, T. D., Bonneville, S., Carslaw, K. S., Mihalopoulos, N., Baker, A. R., and Benning, L. G.: Impacts on iron solubility in the mineral dust by processes in the source region and the atmosphere: A review, *Aeolian Res.*, 5, 21-42, doi: 10.1016/j.aeolia.2012.03.001, 2012.
- 824 Shi, Z., Krom, M. D., Bonneville, S., and Benning, L. G.: Atmospheric processing outside clouds increases soluble iron in mineral dust, *Environ. Sci. Technol.*, 49, 1472-1477, doi: 10.1021/es504623x, 2015.
- 826 Shi, Z. B., Woodhouse, M. T., Carslaw, K. S., Krom, M. D., Mann, G. W., Baker, A. R., Savov, I., Fones, G. R., Brooks, B., Drake, N., Jickells, T. D., and Benning, L. G.: Minor effect of physical size sorting on iron solubility of transported mineral dust, *Atmos. Chem. Phys.*, 11, 8459-8469, doi: 10.5194/acp-11-8459-2011, 2011c.
- 829 Sidhu, P. S., Gilkes, R. J., Cornell, R. M., Posner, A. M., and Quirk, J. P.: Dissolution of Iron Oxides and Oxyhydroxides in Hydrochloric and Perchloric Acids, *Clays Clay Miner.*, 29, 269-276, doi: 10.1346/CCMN.1981.0290404, 1981.
- 831 Spokes, L. J., and Jickells, T. D.: Factors controlling the solubility of aerosol trace metals in the atmosphere and on mixing into seawater, *Aquat. Geochem.*, 1, 355-374, doi: 10.1007/BF00702739, 1995.
- 833 Srinivas, B., Sarin, M. M., and Kumar, A.: Impact of anthropogenic sources on aerosol iron solubility over the Bay of Bengal and the Arabian Sea, *Biogeochemistry*, 110, 257-268, doi: 10.1007/s10533-011-9680-1, 2012.
- 834



- 835 Srinivas, B., and Sarin, M. M.: Atmospheric dry-deposition of mineral dust and anthropogenic trace metals to the Bay of
836 Bengal, *J. Mar. Syst.*, 126, 56-68, doi: 10.1016/j.jmarsys.2012.11.004, 2013.
- 837 Surana, V., and Warren, I.: The leaching of goethite, *Transactions of the Institute of Mining and Metallurgy*, 80, C152-155,
838 1969.
- 839 Sutto, T. E.: Magnetite fine particle and nanoparticle environmental contamination from industrial uses of coal, *Environ. Pollut.*,
840 243, 528-533, doi: 10.1016/j.envpol.2018.08.080, 2018.
- 841 Valeev, D., Mikhailova, A., and Atmadzhidi, A.: Kinetics of Iron Extraction from Coal Fly Ash by Hydrochloric Acid
842 Leaching, *Metals*, 8, 533, doi: 10.3390/met8070533, 2018.
- 843 Valeev, D., Kuniylova, I., Alpatov, A., Varnavskaya, A., and Ju, D.: Magnetite and Carbon Extraction from Coal Fly Ash Using
844 Magnetic Separation and Flotation Methods, *Minerals*, 9, 320, doi: 10.3390/min9050320, 2019.
- 845 Viollier, E., Inglett, P. W., Hunter, K., Roychoudhury, A. N., and Van Cappellen, P.: The ferrozine method revisited:
846 Fe(II)/Fe(III) determination in natural waters, *Appl. Geochem.*, 15, 785-790, doi: 10.1016/s0883-2927(99)00097-9, 2000.
- 847 Waanders, F. B., Vinken, E., Mans, A., and Mulaba-Bafubiandi, A. F.: Iron Minerals in Coal, Weathered Coal and Coal Ash
848 – SEM and Mössbauer Results, *Hyperfine Interact.*, 148, 21-29, doi: 10.1023/B:HYPE.0000003760.89706.f6, 2003.
- 849 Wang, R., Balkanski, Y., Boucher, O., Bopp, L., Chappell, A., Ciais, P., Hauglustaine, D., Penueles, J., and Tao, S.: Sources,
850 transport and deposition of iron in the global atmosphere, *Atmos. Chem. Phys.*, 15, 6247-6270, doi: 10.5194/acp-15-6247-
851 2015, 2015.
- 852 Wang, X. S.: Mineralogical and chemical composition of magnetic fly ash fraction, *Environ. Earth Sci.*, 71, 1673-1681, doi:
853 10.1007/s12665-013-2571-0, 2014.
- 854 Warren, C. J., and Dudas, M. J.: Leachability and partitioning of elements in ferromagnetic fly ash particles, *Sci. Total Environ.*,
855 84, 223-236, doi: 10.1016/0048-9697(89)90385-9, 1989.
- 856 Wexler, A. S., and Clegg, S. L.: Atmospheric aerosol models for systems including the ions H^+ , NH_4^+ , Na^+ , SO_4^{2-} , NO_3^- , Cl^- ,
857 Br^- , and H_2O , *J. Geophys. Res.-Atmos.*, 107, 4207, doi: 10.1029/2001JD000451, 2002.
- 858 Xu, N., and Gao, Y.: Characterization of hematite dissolution affected by oxalate coating, kinetics and pH, *Appl. Geochem.*,
859 23, 783-793, doi: 10.1016/j.apgeochem.2007.12.026, 2008.
- 860 Yao, Z. T., Ji, X. S., Sarker, P. K., Tang, J. H., Ge, L. Q., Xia, M. S., and Xi, Y. Q.: A comprehensive review on the applications
861 of coal fly ash, *Earth-Sci. Rev.*, 141, 105-121, doi: 10.1016/j.earscirev.2014.11.016, 2015.
- 862 Yu, J. Z., Huang, X.-F., Xu, J., and Hu, M.: When Aerosol Sulfate Goes Up, So Does Oxalate: Implication for the Formation
863 Mechanisms of Oxalate, *Environ. Sci. Technol.*, 39, 128-133, doi: 10.1021/es049559f, 2005.
- 864 Zhang, D., Iwasaka, Y., Shi, G., Zang, J., Matsuki, A., and Trochkin, D.: Mixture state and size of Asian dust particles
865 collected at southwestern Japan in spring 2000, *J. Geophys. Res.-Atmos.*, 108, 4760, doi: 10.1029/2003JD003869, 2003.
- 866 Zhao, Y., Zhang, J., Sun, J., Bai, X., and Zheng, C.: Mineralogy, Chemical Composition, and Microstructure of Ferrospheres
867 in Fly Ashes from Coal Combustion, *Energy Fuels*, 20, 1490-1497, doi: 10.1021/ef060008f, 2006.
- 868 Zhu, X. R., Prospero, J. M., Millero, F. J., Savoie, D. L., and Brass, G. W.: The solubility of ferric ion in marine mineral
869 aerosol solutions at ambient relative humidities *Mar. Chem.*, 38, 91-107, doi: 10.1016/0304-4203(92)90069-m, 1992.
- 870